Observing the Chemistry of Cities: Space-based Spectroscopy of NO_2

By

Lukas C. Valin

A dissertation submitted in partial satisfaction of the

requirements for the degree of

Doctor of Philosophy

In

Chemistry

in the

Graduate Division

of the

University of California, Berkeley

Committee in charge:

Professor Ronald C. Cohen, Chair
Professor Kristie A. Boering
Professor Inez Fung

Fall 2012

Abstract

Observing the Chemistry of Cities: Space-based Spectroscopy of NO_2

By

Lukas C. Valin

Doctor of Philosophy in Chemistry

University of California, Berkeley

Professor Ronald Cohen, Chair

The atmospheric chemistry of cities depends strongly on the concentration of the hydroxyl radical (OH). OH removes organic molecules (τ = minutes – days), nitrogen oxides (NO_x: NO + NO_2; τ = 2 – 20 h), and sulfur dioxide (τ = 2 – 3 d) from the atmosphere and forms ozone and particulate matter in the process. The spatial and temporal variability of OH is not fully understood due in large part to its strong nonlinear dependence on the concentration of NO_x. In this dissertation, I use measurements of the NO_2 column from the Ozone Monitoring Instrument (OMI), a satellite-based UV/Visible spectrometer, and calculations from chemical transport models to investigate the relationship of OH and NO_x in urban regions. I characterize the instrumental and model performance necessary to accurately infer OH concentration from space-based measurements of the NO_2 column. I use the OMI observations and the WRF-Chem model to investigate the spatial variability of the NO_2 column over a variety of emission sources. I find, not surprisingly, that a result of the nonlinear dependence of OH on NO_x is that the lifetime of NO_x depends on the spatial distribution of NO_x. Where the nonlinear NO_x-OH feedbacks are most important, I find that a spatial resolution of 4 – 8 km is necessary for both model simulations and measurements to accurately capture variations of the NO_2 column. Although this result is expected, quantitative analyses of the nonlinear coupling were not previously available and the calculations presented in this dissertation serve as a guide to interpretation of coarse-resolution measurements and models. I investigate the response of the NO_2 column observed by OMI to variations of wind speed and day-of-week emission patterns. I find that these high spatial resolution measurements (13×24 km^2 at nadir) contain independent information on both NO_x emissions and removal.

Table of Contents

Acknowledgements

I want to acknowledge those who have made significant contributions to my financial support, academic pursuits and extracurricular activities during my graduate studies at University of California, Berkeley. I want to first give a special thanks to my parents and brothers, whose upbringing and support I have appreciated my entire life and will continue to appreciate. I want to thank my advisor Ron Cohen for the time, thought, care, energy and excitement that he shared each day, and for giving me the freedom to explore new ideas. In Professor Cohen's group, I have had the great pleasure of working with many talented and thoughtful colleagues. I want to especially thank Ashley Russell, Ellie Browne, Sally Pusede, Rynda Hudman, Simon Schmutz, Pascal Tay Ma-lin and Paul Wooldridge for many valuable conversations. I also want to thank my committee members, Kristie Boering and Inez Fung, as well as the Berkeley atmospheric science community at large. I want to thank my undergraduate advisor, Keith Kuwata, whose friendship and interest has continued over the years. Without the generous financial support of the NASA Earth and Science Fellowship program, research grants from NASA and the California Air Resources Board, and university funds, my work would not have been possible. Finally, my time living in downtown Berkeley would certainly not have been as fun or as rich without the company of Ken Ogorzalek, Selim "The Jasmine Dream" Moussa, Golden Krishna, and many others, particularly friends within the College of Chemistry, or without all of the evenings spent playing softball next to the hills of the Clark-Kerr campus. Thank you to all who have contributed to my experiences here in Berkeley!

Chapter 1 – Introduction

The hydroxyl radical (OH) is the most important oxidant in the atmosphere. Its concentration determines the rate of NO_x ($NO + NO_2$) removal, the formation of ozone, the formation of particulate matter, and the oxidation rates of volatile organic compounds (VOC) including CH_4 and CO. Observing OH is difficult, in part due to its reactivity ($\tau_{OH} < 1$ s) and low concentration (< 0.5 part-per-trillion), but also due to the variability of its numerous sources and sinks. The goal that has guided the research presented in this dissertation has been to understand if it is possible to accurately infer the concentration of OH using satellite-based UV/Vis spectroscopy of NO_2 and to describe the instrumental performance and analytical procedures necessary to do so.

NO_x is emitted to the atmosphere by fossil-fuel combustion, biomass burning, soil microbial processes, and lightning. NO_x is removed primarily by reaction of NO_2 with OH, but also by deposition and reactions involving alkyl and acyl peroxy radicals to form alkyl and peroxyacyl nitrates. In the troposphere, NO and NO_2 form a catalytic cycle resulting in production of ozone, which is a cardio-respiratory irritant, a costly hazard to agriculture, and a potent greenhouse gas. Upon reaction with OH, NO_x is converted to nitric acid (HNO_3), which is a major constituent of urban particulate matter, is a cardio-respiratory health-hazard, and contributes to large-scale modifications of the Earth's nitrogen cycle.

The relationship of OH to NO_x is paramount to our understanding of atmospheric composition and processing. The variation of OH concentration is not fully understood, in no small part due to its strong dependence on the concentration of NO_x (Fig. 1.1) and VOC. The concentration of OH is low near a source of NO_x ($NO_x \approx 100$ ppb), high at a plume edge ($NO_x \approx 1$ ppb), and low in the remote atmosphere ($NO_x \approx 100$ ppt). As a consequence, the NO_x lifetime with respect to OH is long near a source, is short at a plume edge, is long in background conditions, and thus depends strongly on the rate at which the source is mixed with the background atmosphere.

Providing spatially-complete, observationally-derived NO_x emissions inventories has long been a goal of research scientists and policy makers. Space-based UV/Vis spectrometers make measurements of sunlight reflected from the Earth's surface. Tropospheric NO_2 column densities are inferred from the measured spectra (e.g., Burrows et al., 1999; Martin et al., 2002; Boersma et al., 2004; Bucsela et al., 2006; Boersma et al., 2007). Recent space-based observations of NO_2 have provided extraordinary new insights into emissions of NO_x associated with lightning (e.g., Beirle et al., 2010; Bucsela et al., 2010), soils (e.g., Jaegle et al., 2005; Ghude et al., 2010; Hudman et al., 2010; Hudman et al., 2012), fires (e.g., Jaegle et al., 2005; Mebust et al., 2011) and anthropogenic activities (e.g., Kim et al., 2009; Russell et al., 2010; Castellanos and Boersma, 2012; Russell et al., 2012). Most of these studies evaluate the observations of NO_2 column using an implicit, or in some cases, explicit, assumption that the chemistry is well understood and that NO_x emissions are the most uncertain parameter (e.g., Martin et al., 2003; Stavrakou et al., 2008; Kim et al., 2009; Lamsal et al., 2011; Miyazaki et al., 2012). However, due to the nonlinear dependence of the NO_x lifetime on the NO_x concentration (Fig. 1.1), this assumption can introduce large errors (see Chapter 3). As a result, using the satellite observations of NO_2 to infer emissions requires an understanding of the OH concentration and its effect on the NO_x lifetime at the spatial scales for which NO_x-OH feedbacks are most important (e.g., as in Fig. 1.2).

In this dissertation, I investigate the maximum spatial resolution possible for measuring atmospheric NO_2 using current space-based UV/Vis spectrometers (Chapter 2) and then investigate the spatial resolution required to accurately infer NO_x emissions from point (e.g., a power plant) and area sources (e.g., a city) using models (Chapter 3). Building on the insights from these chapters and related papers published by my colleague, Ashley Russell (Russell et al., 2010; Russell et al., 2011; Russell et al., 2012), I investigate the effects of wind speed on NO_2 observations and derive a wind-dependent effective OH concentration (Chapter 4). Finally, I investigate the response of urban NO_2 concentrations to weekend NO_x emission reductions, comparing observations to a photochemical model with the aim of understanding why the base model gives such a poor representation of the response of the NO_2 column to emission reductions over the weekend (Chapter 5). The findings highlight the importance of high spatial resolution for both measurements and model simulations and show that the observations contain independent information on both NO_x chemistry and emissions.

In Chapter 2, I investigate the spatial variability of the NO_2 column over a variety of sources, demonstrating that existing space-based instrumentation is capable of capturing variations of the NO_2 column at spatial scales of 7 km. Slant column NO_2 is operationally retrieved from the Ozone Monitoring Instrument (OMI) with a nadir footprint of 13×24 km^2, the result of averaging eight detector elements on the instrument (Dobber et al., 2008). For 85 orbits in late 2004, OMI observations from individual "super-zoom" detector elements (spaced at 13×3 km^2 at nadir) were reported. I retrieve slant column NO_2 from these super-zoom observations. I assess the spatial response of the individual detector elements in-flight and determine an upper-bound on spatial resolution of 9 km, in good agreement with on-ground calibration (7 km FWHM) (Dobber et al., 2008). I determine the precision of the super-zoom mode to be 2.1×10^{15} molecules cm^{-2}, approximately a factor of $\sqrt{8}$ worse than an identical retrieval at operational scale as expected if random noise dominates the uncertainty. Over a large power plant, I find that the super-zoom mode of OMI measures variations in slant column NO_2 a factor of 30 larger than the instrumental precision within one operational footprint, thus demonstrating the large variability in NO_2 that could be observed with routine high spatial resolution measurements that are expected from planned geosynchronous satellite instruments such as TEMPO (launch 2017) and GEO-CAPE (launch 2020).

In Chapter 3, I examine the effects of computing nonlinear NO_x-OH chemistry on a model grid. It is known that species subject to non-linear sources or sinks, such as ozone, are susceptible to biases in coarse-resolution CTMs. I compute the resolution-dependent bias in simulated NO_2 column. I use 1-D and 2-D models to illustrate the mechanisms responsible for biases over a range of NO_2 concentrations and model resolutions. I find that predicted biases are largest at coarsest model resolutions, with negative biases predicted over large sources and positive biases predicted over small sources. I use WRF-Chem as an example to illustrate the resolution necessary to predict 10 AM and 1 PM NO_2 column to 10 and 25% accuracy over three large sources: the Four Corners power plants in northwest New Mexico, the city of Los Angeles, California, and the San Joaquin Valley region in California. I find that resolution in the range of 4–12 km is sufficient to accurately model nonlinear effects in the NO_2 loss rate for these three locations. Higher resolution is needed for point sources than for area sources. These estimates of resolution are likely applicable to other cities as they are a consequence of generic chemistry and urban emission distributions.

In Chapter 4, I investigate the relationship of NO_2, OH and the rate of atmospheric mixing using NO_2 measurements over Riyadh, Saudi Arabia, as a case study. These observations illustrate the nonlinear dependence of the OH concentration on NO_2 and on the rate of atmospheric mixing. I derive a range of NO_x lifetimes of 5.5 hours to 8.0 hours, lifetimes that correspond to an effective plume-averaged OH concentration of 7.6×10^6 molecules cm^{-3} at fast (26 km hr^{-1}) and 5.2×10^6 molecules cm^{-3} at slow (4 km hr^{-1}) wind speeds.

In Chapter 5, I explore the relationship of NO_2, OH, and day-of-week variations of NO_x emissions over Los Angeles. For a large source of NO_x, a decrease of NO_x emissions results in increased OH concentration and, consequently, a shorter NO_x lifetime (Fig. 1.1). I examine spatial variations in the day-of-week pattern of the NO_2 column over the Los Angeles metropolitan area using OMI and then compare the observations to calculations using the WRF-Chem model. Over Los Angeles, OMI measures a large decrease of the NO_2 column on the weekends relative to the weekdays (~40%). The observed decreases are not spatially uniform. Over downtown Los Angeles, where NO_2 columns are maximum, weekend decreases are less than 35% but are as large as 60% downwind over the San Bernardino Valley. In a base model, I simulate the weekend effect by decreasing NO_x emissions uniformly by 37.5%. In the base model, simulated decreases are in qualitative agreement with the observed pattern, but are larger over central Los Angles and are smaller over the San Bernardino Valley. I find that the magnitude and spatial pattern of the day-of-week variations of the NO_2 column are more accurately simulated when I adjust the lifetime of NO_x with respect to OH and RO_2 and when I alter the spatial and temporal pattern of weekend emissions. These improvements suggest that constraints on the processes affecting urban photochemistry using space-based observations are possible at a level of detail not previously appreciated.

The future of space-based observations of surface-layer atmospheric chemistry is bright. In Chapters 2 – 5, I investigate the relationship between the concentration of OH and the NO_2 column with respect to variations of NO_x distribution, emission rate, and the speed of the wind. In Chapter 6, I describe new ideas for future research with current instrumentation and provide an outline of what will become possible with the launch of geosynchronous-based UV/Vis instruments.

References

Beirle, S., Huntrieser, H., and Wagner, T.: Direct satellite observation of lightning-produced NO_x, Atmospheric Chemistry and Physics, 10, 10965-10986, 10.5194/acp-10-10965-2010, 2010.

Boersma, K. F., Eskes, H. J., and Brinksma, E. J.: Error analysis for tropospheric NO_2 retrieval from space, Journal of Geophysical Research-Atmospheres, 109, D04311, 2004

Boersma, K. F., Eskes, H. J., Veefkind, J. P., Brinksma, E. J., van der A, R. J., Sneep, M., van den Oord, G. H. J., Levelt, P. F., Stammes, P., Gleason, J. F., and Bucsela, E. J.: Near-real time retrieval of tropospheric NO_2 from OMI, Atmospheric Chemistry and Physics, 7, 2103-2118, 2007.

Bucsela, E. J., Celarier, E. A., Wenig, M. O., Gleason, J. F., Veefkind, J. P., Boersma, K. F., and Brinksma, E. J.: Algorithm for NO_2 vertical column retrieval from the Ozone Monitoring Instrument, IEEE Transactions on Geoscience and Remote Sensing, 44, 1245-1258, 10.1109/tgrs.2005.863715, 2006.

Bucsela, E. J., Pickering, K. E., Huntemann, T. L., Cohen, R. C., Perring, A., Gleason, J. F., Blakeslee, R. J., Albrecht, R. I., Holzworth, R., Cipriani, J. P., Vargas-Navarro, D., Mora-Segura, I., Pacheco-Hernandez, A., and Laporte-Molina, S.: Lightning-generated NO_x seen by the Ozone Monitoring Instrument during NASA's Tropical Composition, Cloud and Climate Coupling Experiment (TC4), Journal of Geophysical Research-Atmospheres, 115, 2010.

Burrows, J. P., Weber, M., Buchwitz, M., Rozanov, V., Ladstatter-Weissenmayer, A., Richter, A., DeBeek, R., Hoogen, R., Bramstedt, K., Eichmann, K. U., and Eisinger, M.: The Global Ozone Monitoring Experiment (GOME): Mission concept and first scientific results, Journal of the Atmospheric Sciences, 56, 151-175, 1999.

Castellanos, P., and Boersma, K. F.: Reductions in nitrogen oxides over Europe driven by environmental policy and economic recession, Scientific Reports, 2, 7, 2012.

Dobber, M., Kleipool, Q., Dirksen, R., Levelt, P., Jaross, G., Taylor, S., Kelly, T., Flynn, L., Leppelmeier, G., and Rozemeijer, N.: Validation of Ozone Monitoring Instrument Level 1B data products, Journal of Geophysical Research-Atmospheres, 113, D15s06, 2008.

Ghude, S. D., Lal, D. M., Beig, G., van der A, R., and Sable, D.: Rain-Induced Soil NO_x Emission From India During the Onset of the Summer Monsoon: A Satellite Perspective, Journal of Geophysical Research-Atmospheres, 115, 9, 2010.

Hudman, R. C., Russell, A. R., Valin, L. C., and Cohen, R. C.: Interannual variability in soil nitric oxide emissions over the United States as viewed from space, Atmospheric Chemistry and Physics, 10, 9943-9952, 2010.

Hudman, R. C., Moore, N. E., Mebust, A. K., Martin, R. V., Russell, A. R., Valin, L. C., and Cohen, R. C.: Steps towards a mechanistic model of global soil nitric oxide emissions: implementation and space based-constraints, Atmospheric Chemistry and Physics, 12, 7779-7795, 2012.

Jaegle, L., Steinberger, L., Martin, R. V., and Chance, K.: Global partitioning of NO_x sources using satellite observations: Relative roles of fossil fuel combustion, biomass burning and soil emissions, Faraday Discussions, 130, 407-423, 2005.

Kim, S. W., Heckel, A., Frost, G. J., Richter, A., Gleason, J., Burrows, J. P., McKeen, S., Hsie, E. Y., Granier, C., and Trainer, M.: NO_2 columns in the western United States observed from space and simulated by a regional chemistry model and their implications for NO_x emissions, Journal of Geophysical Research-Atmospheres, 114, 29, D11301, 2009.

Lamsal, L. N., Martin, R. V., Padmanabhan, A., van Donkelaar, A., Zhang, Q., Sioris, C. E., Chance, K., Kurosu, T. P., and Newchurch, M. J.: Application of satellite observations for timely updates to global anthropogenic NO_x emission inventories, Geophysical Research Letters, 38, 2011.

Martin, R. V., Chance, K., Jacob, D. J., Kurosu, T. P., Spurr, R. J. D., Bucsela, E., Gleason, J. F., Palmer, P. I., Bey, I., Fiore, A. M., Li, Q. B., Yantosca, R. M., and Koelemeijer, R. B. A.: An improved retrieval of tropospheric nitrogen dioxide from GOME, Journal of Geophysical Research-Atmospheres, 107, 4437, 2002.

Martin, R. V., Jacob, D. J., Chance, K., Kurosu, T. P., Palmer, P. I., and Evans, M. J.: Global inventory of nitrogen oxide emissions constrained by space-based observations of NO_2 columns, Journal of Geophysical Research-Atmospheres, 108, 4537, 2003.

Mebust, A. K., Russell, A. R., Hudman, R. C., Valin, L. C., and Cohen, R. C.: Characterization of wildfire NO_x emissions using MODIS fire radiative power and OMI tropospheric NO_2 columns, Atmospheric Chemistry and Physics, 11, 5839-5851, 2011.

Miyazaki, K., Eskes, H. J., and Sudo, K.: Global NO_x emission estimates derived from an assimilation of OMI tropospheric NO_2 columns, Atmospheric Chemistry and Physics, 12, 2263-2288, 2012.

Russell, A., Valin, L., and Cohen, R.: Trends in OMI NO_2 observations over the US: effects of emission control technology and the economic recession, Atmospheric Chemistry and Physics Discussions, 12, 15419-15452, 2012.

Russell, A. R., Valin, L. C., Bucsela, E. J., Wenig, M. O., and Cohen, R. C.: Space-based Constraints on Spatial and Temporal Patterns of NO_x Emissions in California, 2005-2008, Environmental Science & Technology, 44, 3608-3615, 2010.

Russell, A. R., Perring, A. E., Valin, L. C., Bucsela, E. J., Browne, E. C., Min, K. E., Wooldridge, P. J., and Cohen, R. C.: A high spatial resolution retrieval of NO_2 column densities from OMI: method and evaluation, Atmospheric Chemistry and Physics, 11, 8543-8554, 2011.

Stavrakou, T., Muller, J. F., Boersma, K. F., De Smedt, I., and van der A, R. J.: Assessing the distribution and growth rates of NO_x emission sources by inverting a 10-year record of NO_2 satellite columns, Geophysical Research Letters, 35, 2008.

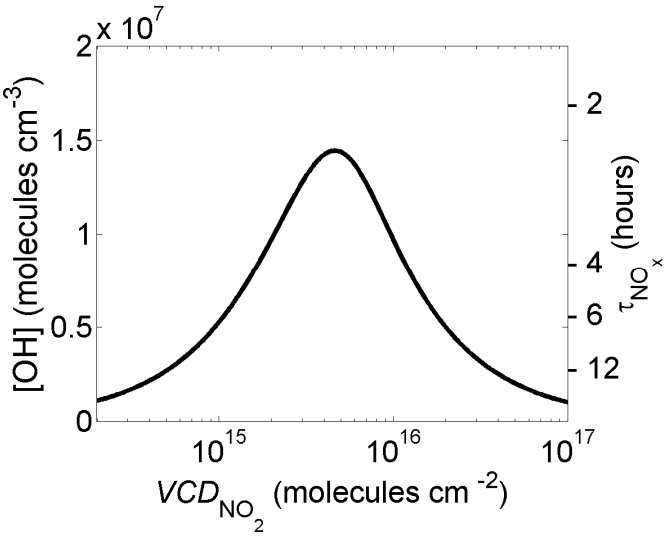

Figure 1.1 The steady-state concentration of OH versus the concentration of NO_x for conditions typical of a polluted urban environment. The lifetime of NO_x with respect to reaction of NO_2 with OH is indicated on the right axis, assuming an NO_2 to NO_x ratio of 0.72.

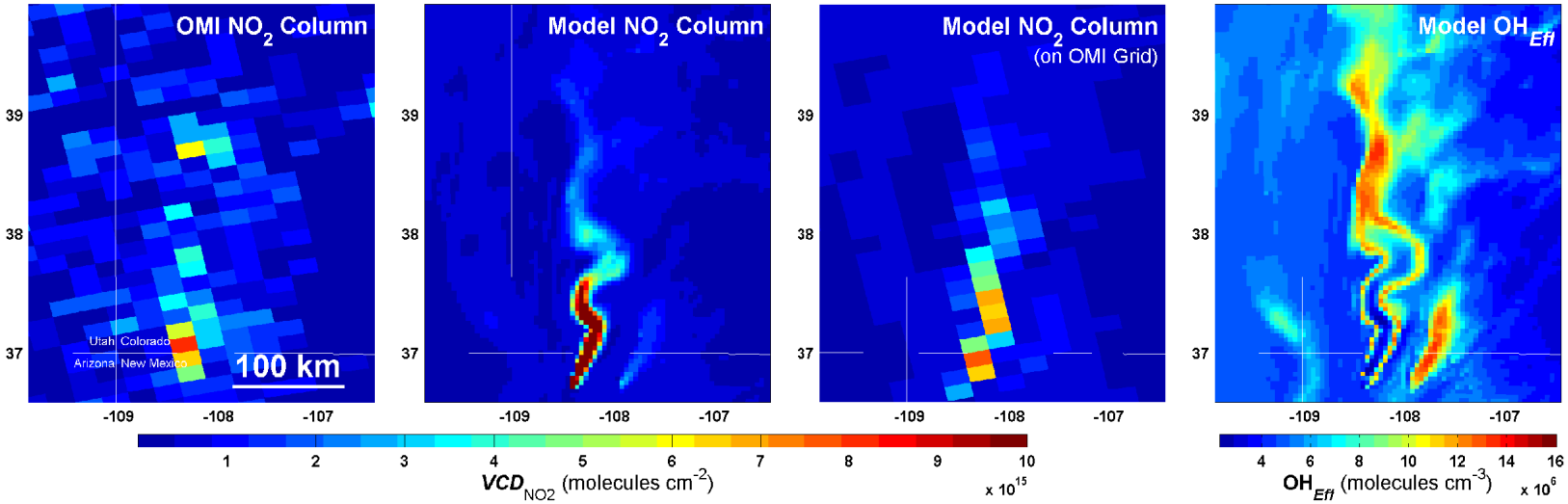

Figure 1.2 NO_2 column on 27 May 2006 over Four Corners Power Plant observed by OMI (left panel), simulated by WRF-Chem (second panel), the same simulation but sampled on the OMI grid (third panel), and the effective OH concentration simulated by WRF-Chem (right panel). The effective OH concentration is the NO_2-weighted average OH concentration integrated over the full vertical column. Accurate representation of NO_2 spatial patterns is necessary to accurately simulate the concentration of OH.

Chapter 2 – Observation of slant column NO_2 using the super-zoom mode of AURA-OMI

2.1 Introduction

Nitrogen oxides ($NO_x \equiv NO + NO_2$) exhibit strong control over tropospheric ozone production and HO_x ($HO_2 + RO_2 + HO$) cycling. Despite a relatively short chemical lifetime ($\tau_{NOx} \sim 1.5$ h − 1 day in the planetary boundary layer), NO_x emitted locally can result in perturbations to atmospheric composition that extend for hundreds of kilometers, in part due to atmospheric processing that stores and releases NO_x, but also in part due to the magnitude of the source being many e-folds in excess of the global background.

Satellite-based UV/Visible mapping spectrometers provide a comprehensive view of the global and regional patterns of NO_2 columns (e.g., Jaegle et al., 2005; Richter et al., 2005; Russell et al., 2010). Interpretation of these observations has primarily been via chemical transport models (grid spacing ≈ 100 km) that assume chemical processing is accurately represented (e.g. Martin et al., 2003; Toenges-Schuller et al., 2006; Konovalov et al., 2006; Kim et al., 2006). Many of these models have resolution that is coarse compared to both the e-folding decay length of an NO_2 plume and the spatial resolution provided by the satellite instruments. High resolution observations offer the possibility of direct measurement of the spatial gradients in the NO_2 column in regions where such gradients depend on the chemical loss rates of NO_2 more strongly than on emissions (e.g. Heue et al., 2008). The resolution needed for such analyses is still a subject of research (e.g. Loughner et al., 2007; Valin et al., 2011); however, it seems likely to be in the range of 3–10 km.

Here I use observations from OMI (Levelt et al., 2006a, b) to retrieve slant column NO_2 at high spatial resolution. I test the spatial resolution of the OMI super-zoom mode, assess the uncertainty of super-zoom observations, and then retrieve slant column NO_2 over several source types. I discuss the implications of the enhanced spatial resolution on our understanding of NO_x emission sources and the variability of atmospheric NO_2 using observations of Dubai, UAE.

2.2 Methods

OMI sits aboard the sun-synchronous, polar-orbiting NASA Aura satellite (Schoeberl et al., 2006), measuring solar and backscattered UV/Visible radiance with a standard operational footprint of 24 × 13 km^2 at nadir, an average of eight detector elements (Levelt et al., 2006a,b). OMI also has the ability to operate in a super-zoom mode where the detector elements are not averaged on board. From 1 October 2004 to 31 December 2004, OMI performed 85 super-zoom orbits, 42 of which reported observations at nadir. Due to data transmission constraints, this increase in spatial sampling requires a corresponding decrease in spatial coverage such that a single super-zoom nadir orbit covers only 180 km of the 2600 km operational-mode swath width.

I use the level 1b calibrated, wavelength-corrected OMI radiance (OML1BRVZ, OML1BRVG v.3) and solar irradiance (OML1BRR v.3) data recorded on the Goddard Earth Sciences Data and Information Services Center (GES-DISC, http://disc.sci.gsfc.nasa.gov/Aura/data-holdings/OMI) (Van den Oord et al., 2006; Dobber et al., 2008). Observed earthshine spectra are divided by the average of solar spectra from 2005 to obtain top-of-atmosphere reflectance spectra. It has been shown that the averaging of solar spectra reduces noise and detector anomalies known as “striping” in the NO_2 retrieval (Celarier et al., 2008; Dobber et al., 2008). I apply a de-striping algorithm to retrieved slant column NO_2 following Boersma et al. (2007).

I have attempted to emulate the operational retrievals (Boersma et al., 2007; Bucsela et al., 2006). I retrieve slant column NO_2 by performing a DOAS linear least squares fit (Platt and Stutz, 2008; Wenig et al., 2005) of an NO_2 cross section (Vandaele et al., 2002), an O_3 cross section (Bogumil et al., 2001), a Ring spectrum (Chance and Spurr, 1997; Chance and Kurucz, 2010), a water vapor cross section (Harder and Brault, 1997), and a third-order polynomial to the logarithm of the observed reflectance. I perform the fit over the 405–465 nm spectral window.

2.3 Spatial resolution of OMI super-zoom mode

On-ground calibration measurements determined the footprint of a point light source to be near-Gaussian, spanning 2.3 detector row elements at nadir (7 km FWHM) (Dobber et al., 2006). To determine an in-flight value, I compare the decay of MODIS and OMI broadband (459–479 nm) top-of-atmosphere reflectance over the Qatari coastline on 19 November 2004 (Fig. 2.1). MODIS reflectance is reported at a resolution of 500×500 m^2. By comparing the MODIS and OMI observed reflectance across a sharp transition, such as a coastline, I can deduce a value for the spatial resolution of OMI. For a single transect, MODIS observations decrease in normalized reflectance from 0.8 to 0.2 over 3 km, a decrease that OMI observes over 9 km. Additionally, the width of an observed enhancement in NO_2 directly over and downwind of an isolated NO_x source is no wider than 6–9 km FWHM (PP4, Fig. 2.2b). Both of these in-flight tests provide an upper bound on instrumental spatial resolution that is in good agreement with on-ground calibration (Dobber et al., 2006).

2.4 Uncertainty in slant column NO_2

Figure 2.2 shows slant column NO_2 retrieved over the Arabian Peninsula and the Indian Ocean from a super-zoom mode orbit on 21 November 2004. To assess the uncertainty in retrieved slant column NO_2, I use a method similar to Boersma et al. (2007). I find that slant column NO_2 retrieved at operational resolution is normally distributed with 1 σ variability of 0.8×10^{15} molecules cm^{-2} over the remote ocean and 0.6×10^{15} molecules cm^{-2} over the remote desert, well within the range of values determined previously (Boersma et al., 2007). The precision of slant column NO_2 retrieved from the super-zoom mode is approximately a factor of $\sqrt{8}$ worse, which is expected for a system with 8 fewer measurements and dominated by random noise.

The NO_2 fit error computed from DOAS residuals does not increase by a factor of $\sqrt{8}$ for super-zoom observations (not shown) indicating that there are systematic residuals not reduced by averaging. While the origin of these systematic residuals is unknown, I speculate that there is slight spectral misalignment in the DOAS fitting procedure. One possible explanation for this misalignment is the lack of a shift and squeeze adjustment to improve the spectral calibration of individual spectra. However, the magnitude of any uncertainty that remains is negligible in comparison to the signal observed over sources of interest (Fig. 2.3)

2.5 Slant column NO_2 from OMI super-zoom mode

To illustrate performance of OMI in super-zoom mode and to indicate the potential for new science to emerge with high spatial resolution observations, I retrieve slant column NO_2 over the Rihand Reservoir in India, Seoul, South Korea and Sarni, Madhya Pradesh, India (Table 1). These regions highlight the super-zoom observations over a set of large point sources (Rihand), a megacity (Seoul), and a small point source (Sarni). I compare the super-zoom observations to the average of six operational- scale overpasses retrieved in the same manner. These operational

resolution observations were made between the months of October and December from 2005–2007 on days when the selected region was cloud-free and nadir to the spacecraft (Table 2.1). I use MODIS reflectance observations, taken aboard the Aqua platform, to serve as independent visual confirmation that the selected scenes are cloud-free.

Over the Rihand Reservoir (Fig. 2.3, a–d), the super-zoom mode distinguishes three maxima in slant column NO_2 directly over or slightly downwind of three large coal-fired power plants. This variability is not detectable with the 24×13 km^2 operational footprint, which only observes one local maximum. Within a single operational-scale footprint, the super-zoom mode observes variation of up to 6.1×10^{16} molecules cm^{-2}, nearly 30 times larger than the instrumental precision over the remote ocean. In the average of six operational-scale observations, the spatial detail is increased, but the spatial contrast observed (Fig. 2.3d, $1\ \sigma = 0.6 \times 10^{16}$ molecules cm^{-2}) is a factor of 2.3 less than that observed by the super-zoom mode (Fig. 2.3b, $1\ \sigma = 1.4 \times 10^{16}$ molecules cm^{-2}). Furthermore, the six-orbit average is only able to distinguish one maximum that is 2 times smaller than that observed on a single day.

Over Seoul, Korea (Fig. 2.3, e–h), a maximum in slant column NO2 (Fig. 2.3f) is observed approximately 12 km to the east of downtown Seoul with the signal decreasing from the maximum to near-background over a distance of 30-50 km. While the operational-scale retrieval captures the general structure of the Seoul urban plume (Fig. 2.3g), the super-zoom mode captures variation of slant column NO_2 of up to 3×10^{16} molecules cm^{-2} (50 %) within a single operational-scale pixel. The six-orbit operational-resolution average (Fig. 2.3h) is much smoother than that observed in a single day, an effect of variable daily meteorology that smoothes the average.

Super-zoom observations capture a maximum in slant column NO_2 directly to the south of the Satpura Power Plant in Sarni, India (Fig. 2.3j; 2.2×10^{16} molecules cm^{-2}), a value that is seven times larger than the variability and average observed over the remote ocean on the same overpass. At operational-scale, both single- and six-orbit average (Fig. 2.3, k–l), the enhancement is modest relative to the surrounding background (~20 %). These observations demonstrate that the instrumental noise of OMI is not the limiting factor in producing high spatial resolution maps of atmospheric NO_2 over megacities and large power plants, or in accurately identifying the location of relatively small NO_x emission sources.

2.6 Case study over Dubai, UAE

In Figure 2.4, I compare slant column NO_2 retrieved from a super-zoom overpass of Dubai with that retrieved from six operational-resolution overpasses (Table 2.1). I choose Dubai because the dataset is relatively simple to interpret. Dubai is an isolated source of NO_x advected over a highly reflective, relatively homogenous desert surface. The observed NO_2 enhancement is approximately 75 km SW–NE by 40 km SE–NW (Fig. 2.4c), about two times the size of the Dubai metropolitan area (Fig. 2.4b). Within the observed plume, slant column NO_2 is highly variable, with differences as much as 2×10^{16} molecules cm^{-2} (~50 %) over 4 cross-track pixels (12 km) or one row (13 km). Adding confidence to the super-zoom observations, the 6-day operational resolution average (Fig. 2.4d) captures the same shape of the plume (75×40 km^2), but is not able to capture the strong gradients observed by the super-zoom mode, the result of a coarser footprint and meteorological variability in the six-day average.

Due to the alignment of the OMI super-zoom footprint, variability of emissions along the Dubai coastline should be detectable. For example, the super-zoom mode observes an

enhancement of slant column NO_2 directly over and downwind from the Jebel Ali Free Trade Zone (JAFTZ), a port and power generation center (A, B, Fig. 2.4, b– c). The enhancement directly over JAFTZ (A) is not as large as the enhancement downwind (B) because the source is near the leeward edge of the 13 km OMI pixel, which dilutes the signal with that of the clean marine background. In addition, the winds were stagnant between 10:00 a.m. and noon, during which NO_2 presumably accumulated over the source (A) and was transported downwind (B) when the winds shifted inland at midday (3 m s^{-1}, 11 km h^{-1}). The six-day area-weighted average (Fig. 2.4d) is not able to distinguish JAFTZ from the dense urban core to the northeast.

These examples demonstrate a few advantages of utilizing measurements at higher spatial resolution than the current OMI (24 × 13 km^2) or GOME-2 (80 × 40 km^2) products. Future opportunities to provide this substantial advance in scientific capability include the proposed TROPOMI (7 × 7 km^2) (Veefkind et al., 2011) and GEOCAPE instruments (currently targeted at 8 × 8 km^2 or 4 × 4 km^2) (NRC, 2007). Such observations will enable the tracking of individual source regions within cities and allow for better assessment of chemistry in urban outflow.

2.7 Conclusions

I show that slant column NO_2 retrieved from the super-zoom mode of OMI captures significant spatial variability at scales much finer than the 24 × 13 km^2 operational footprint. I show that the uncertainty of the super-zoom observations is a factor of $\sqrt{8}$ larger than that retrieved at operational scale, which is expected for 8 times fewer measurements dominated by random error. I take advantage of enhanced resolution of the super-zoom observations to distinguish large point sources near the Rihand Reservoir and to distinguish the Jebel Ali Free Trade Zone, a Dubai port and power generation center, from the Dubai urban center 30 km to the northeast.

References

Earth Science and Applications from Space: National Imperatives for the Next Decade and Beyond, edited by: National Reasearch Council of the National Academies, The National Academies Press, Washington, D.C., 2007.

Boersma, K. F., Eskes, H. J., Veefkind, J. P., Brinksma, E. J., van der A, R. J., Sneep, M., van den Oord, G. H. J., Levelt, P. F., Stammes, P., Gleason, J. F., and Bucsela, E. J.: Near-real time retrieval of tropospheric NO_2 from OMI, Atmospheric Chemistry and Physics, 7, 2103-2118, 2007.

Bogumil, K., Orphal, J., Burrows, J. P., and Flaud, J. M.: Vibrational progressions in the visible and near-ultraviolet absorption spectrum of ozone, Chemical Physics Letters, 349, 241-248, 2001.

Bucsela, E. J., Celarier, E. A., Wenig, M. O., Gleason, J. F., Veefkind, J. P., Boersma, K. F., and Brinksma, E. J.: Algorithm for NO_2 vertical column retrieval from the ozone monitoring instrument, Ieee Transactions on Geoscience and Remote Sensing, 44, 1245-1258,, 2006.

Celarier, E. A., Brinksma, E. J., Gleason, J. F., Veefkind, J. P., Cede, A., Herman, J. R., Ionov, D., Goutail, F., Pommereau, J. P., Lambert, J. C., van Roozendael, M., Pinardi, G., Wittrock, F., Schonhardt, A., Richter, A., Ibrahim, O. W., Wagner, T., Bojkov, B., Mount, G., Spinei, E., Chen, C. M., Pongetti, T. J., Sander, S. P., Bucsela, E. J., Wenig, M. O., Swart, D. P. J., Volten, H., Kroon, M., and Levelt, P. F.: Validation of ozone monitoring instrument nitrogen dioxide columns, Journal of Geophysical Research-Atmospheres, 113, D15s15, 2008.

Chance, K., and Kurucz, R. L.: An improved high-resolution solar reference spectrum for earth's atmosphere measurements in the ultraviolet, visible, and near infrared, Journal of Quantitative Spectroscopy & Radiative Transfer, 111, 1289-1295, 2010.

Chance, K. V., and Spurr, R. J. D.: Ring effect studies: Rayleigh scattering, including molecular parameters for rotational Raman scattering, and the Fraunhofer spectrum, Applied Optics, 36, 5224-5230, 1997.

Dobber, M., Kleipool, Q., Dirksen, R., Levelt, P., Jaross, G., Taylor, S., Kelly, T., Flynn, L., Leppelmeier, G., and Rozemeijer, N.: Validation of Ozone Monitoring Instrument level 1b data products, Journal of Geophysical Research-Atmospheres, 113, D15s06, 2008.

Dobber, M. R., Dirksen, R. J., Levelt, P. F., Van den Oord, G. H. J., Voors, R. H. M., Kleipool, Q., Jaross, G., Kowalewski, M., Hilsenrath, E., Leppelmeier, G. W., de Vries, J., Dierssen, W., and Rozemeijer, N. C.: Ozone-Monitoring Instrument calibration, IEEE Transactions on Geoscience and Remote Sensing, 44, 1209-1238, 2006.

Harder, J. W., and Brault, J. W.: Atmospheric measurements of water vapor in the 442-nm region, Journal of Geophysical Research-Atmospheres, 102, 6245-6252, 1997.

Heue, K. P., Wagner, T., Broccardo, S. P., Walter, D., Piketh, S. J., Ross, K. E., Beirle, S., and Platt, U.: Direct observation of two dimensional trace gas distributions with an airborne Imaging DOAS instrument, Atmospheric Chemistry and Physics, 8, 6707-6717, 2008.

Jaegle, L., Steinberger, L., Martin, R. V., and Chance, K.: Global partitioning of NO_x sources using satellite observations: Relative roles of fossil fuel combustion, biomass burning and soil emissions, Faraday Discussions, 130, 407-423, 2005.

Kim, S. W., Heckel, A., Frost, G. J., Richter, A., Gleason, J., Burrows, J. P., McKeen, S., Hsie, E. Y., Granier, C., and Trainer, M.: NO_2 columns in the western United States observed from space and simulated by a regional chemistry model and their implications for NO_x emissions, Journal of Geophysical Research-Atmospheres, 114, 29, D11301, 2009.

Konovalov, I. B., Beekmann, M., Richter, A., and Burrows, J. P.: Inverse modelling of the spatial distribution of NO_x emissions on a continental scale using satellite data, Atmospheric Chemistry and Physics, 6, 1747-1770, 2006.

Levelt, P. F., Hilsenrath, E., Leppelmeier, G. W., van den Oord, G. H. J., Bhartia, P. K., Tamminen, J., de Haan, J. F., and Veefkind, J. P.: Science objectives of the Ozone Monitoring Instrument, Ieee Transactions on Geoscience and Remote Sensing, 44, 1199-1208, 2006a.

Levelt, P. F., Van den Oord, G. H. J., Dobber, M. R., Malkki, A., Visser, H., de Vries, J., Stammes, P., Lundell, J. O. V., and Saari, H.: The Ozone Monitoring Instrument, Ieee Transactions on Geoscience and Remote Sensing, 44, 1093-1101, 2006b.

Loughner, C. P., Lary, D. J., Sparling, L. C., Cohen, R. C., DeCola, P., and Stockwell, W. R.: A method to determine the spatial resolution required to observe air quality from space, Ieee Transactions on Geoscience and Remote Sensing, 45, 1308-1314, 2007.

Martin, R. V., Jacob, D. J., Chance, K., Kurosu, T. P., Palmer, P. I., and Evans, M. J.: Global inventory of nitrogen oxide emissions constrained by space-based observations of NO_2 columns, Journal of Geophysical Research-Atmospheres, 108, 4537, 2003.

Platt, U., and Stutz, J.: Differential optical absorption spectroscopy principles and applications, Physics of earth and space environments,, Springer Verlag, Berlin, xv, 597 pp., 2008.

Richter, A., Burrows, J. P., Nuss, H., Granier, C., and Niemeier, U.: Increase in tropospheric nitrogen dioxide over China observed from space, Nature, 437, 129-132, 2005.

Russell, A. R., Valin, L. C., Bucsela, E. J., Wenig, M. O., and Cohen, R. C.: Space-based Constraints on Spatial and Temporal Patterns of NO_x Emissions in California, 2005-2008, Environmental Science & Technology, 44, 3608-3615, 2010.

Schoeberl, M. R., Douglass, A. R., Hilsenrath, E., Bhartia, P. K., Beer, R., Waters, J. W., Gunson, M. R., Froidevaux, L., Gille, J. C., Barnett, J. J., Levelt, P. E., and DeCola, P.: Overview of the EOS Aura Mission, Ieee Transactions on Geoscience and Remote Sensing, 44, 1066-1074, 2006.

Toenges-Schuller, N., Stein, O., Rohrer, F., Wahner, A., Richter, A., Burrows, J. P., Beirle, S., Wagner, T., Platt, U., and Elvidge, C. D.: Global distribution pattern of anthropogenic nitrogen oxide emissions: Correlation analysis of satellite measurements and model calculations, Journal of Geophysical Research-Atmospheres, 111, D05312, 2006.

Valin, L., Russell, A., Hudman, R., and Cohen, R.: Effects of model resolution on the interpretation of satellite NO_2 observations, Atmospheric Chemistry and Physics, 11, 11647-11655, 2011.

Van den Oord, G. H. J., Rozemeijer, N. C., Schenkelaars, V., Levelt, P. F., Dobber, M. R., Voors, R. H. M., Claas, J., De Vries, J., Ter Linden, M., De Haan, C., and de Berg, T. V.: OMI level 0 to 1b processing and operational aspects, Ieee Transactions on Geoscience and Remote Sensing, 44, 1380-1397, 2006.

Vandaele, A. C., Hermans, C., Fally, S., Carleer, M., Colin, R., Merienne, M. F., Jenouvrier, A., and Coquart, B.: High-resolution Fourier transform measurement of the NO_2 visible and near-infrared absorption cross sections: Temperature and pressure effects, Journal of Geophysical Research-Atmospheres, 107, 4348, 2002.

Veefkind, J. P., Aben, I., McMullan, K., Forster, H., de Vries, J., Otter, G., Claas, J., Eskes, H. J., de Haan, J. F., Kleipool, Q., van Weele, M., Hasekamp, O., Hoogeveen, R., Landgraf, J., Snel, R., Tol, P., Ingmann, P., Voors, R., Kruizinga, B., Vink, R., Visser, H., and Levelt, P. F.: TROPOMI on the ESA Sentinel-5 Precursor: A GMES mission for global observations of the atmospheric composition for climate, air quality and ozone layer applications, Remote Sensing of Environment, 120, 70-83, 2012.

Wenig, M., Jahne, B. J., and Platt, U.: Operator representation as a new differential optical absorption spectroscopy formalism, Applied Optics, 44, 3246-3253, 2005.

Table 2.1 Dates and regions for which slant column NO_2 was retrieved.

	Rihand, India	**Seoul,** South Korea	**Sarni,** India	**Dubai,** UAE
Region	82.5-83.5° E 23.6-24.5° N	126.7-127.7° E 37.05-37.95° N	77.7-78.7° E 21.5-22.5° N	55.0-55.7° E 24.9-25.5° N
Date of Super Zoom Observations	2004.11.23	2004.11.21	2004.11.19	2004.11.21
Dates in six-orbit average	2005.11.01 2005.11.10 2005.11.17 2005.11.19 2005.11.26 2005.12.05	2005.10.23 2005.11.08 2006.10.12 2006.11.11 2006.11.20 2007.11.07	2005.10.30 2005.11.06 2005.11.22 2005.12.08 2006.11.18 2006.12.11	2005.10.23 2005.10.30 2005.11.01 2005.11.08 2005.12.01 2005.12.03

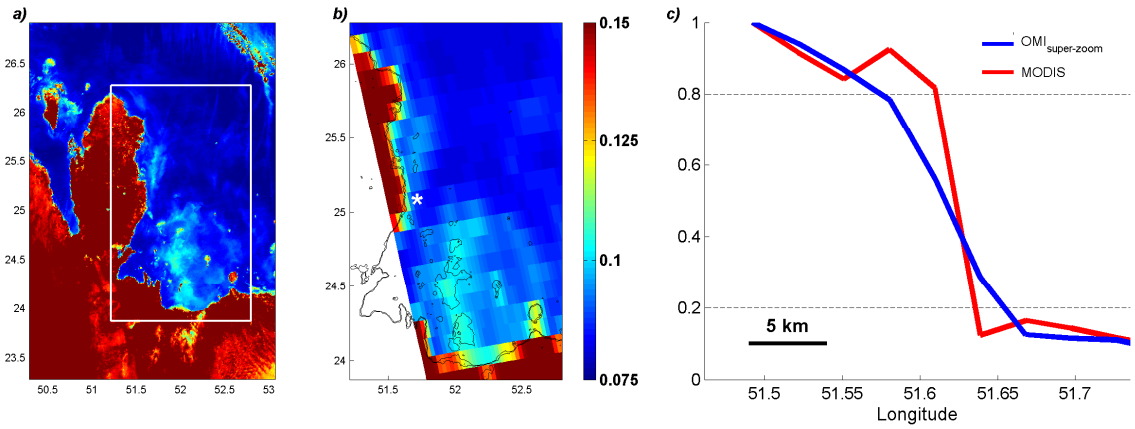

Figure 2.1 Top-of-atmosphere reflectance (459–479 nm) observed by (a) MODIS and (b) the super-zoom mode of OMI over Qatar on 19 November 2004. (c) Normalized top-of-atmosphere reflectance observed by MODIS (red) and OMI (blue) along a transect perpendicular to the Qatari coastline – white boxes, (a–b).

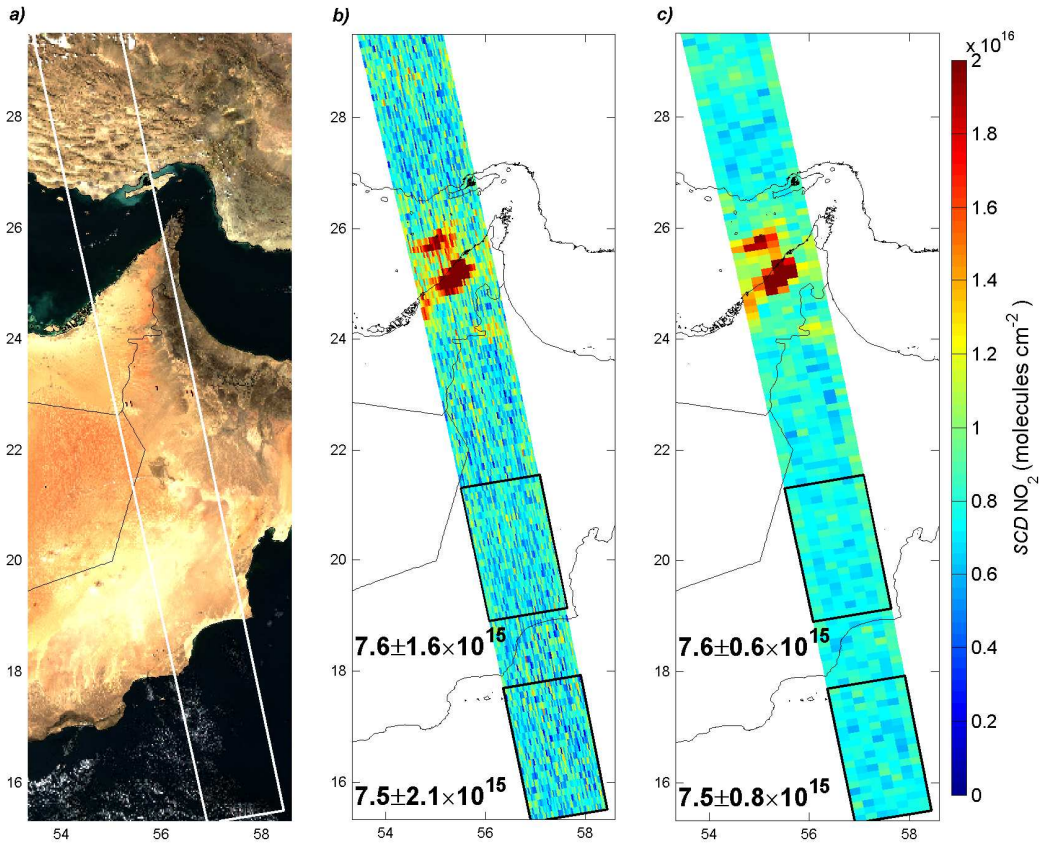

Figure 2.2 (a) MODIS RGB image, (b) super-zoom slant column NO_2, and (c) operational-scale slant column NO_2 over the eastern Arabian Peninsula on 21 November 2004. The mean and 1–σ uncertainty of slant column NO_2 retrieved from super-zoom and operational-scale observations over the remote ocean and desert are reported.

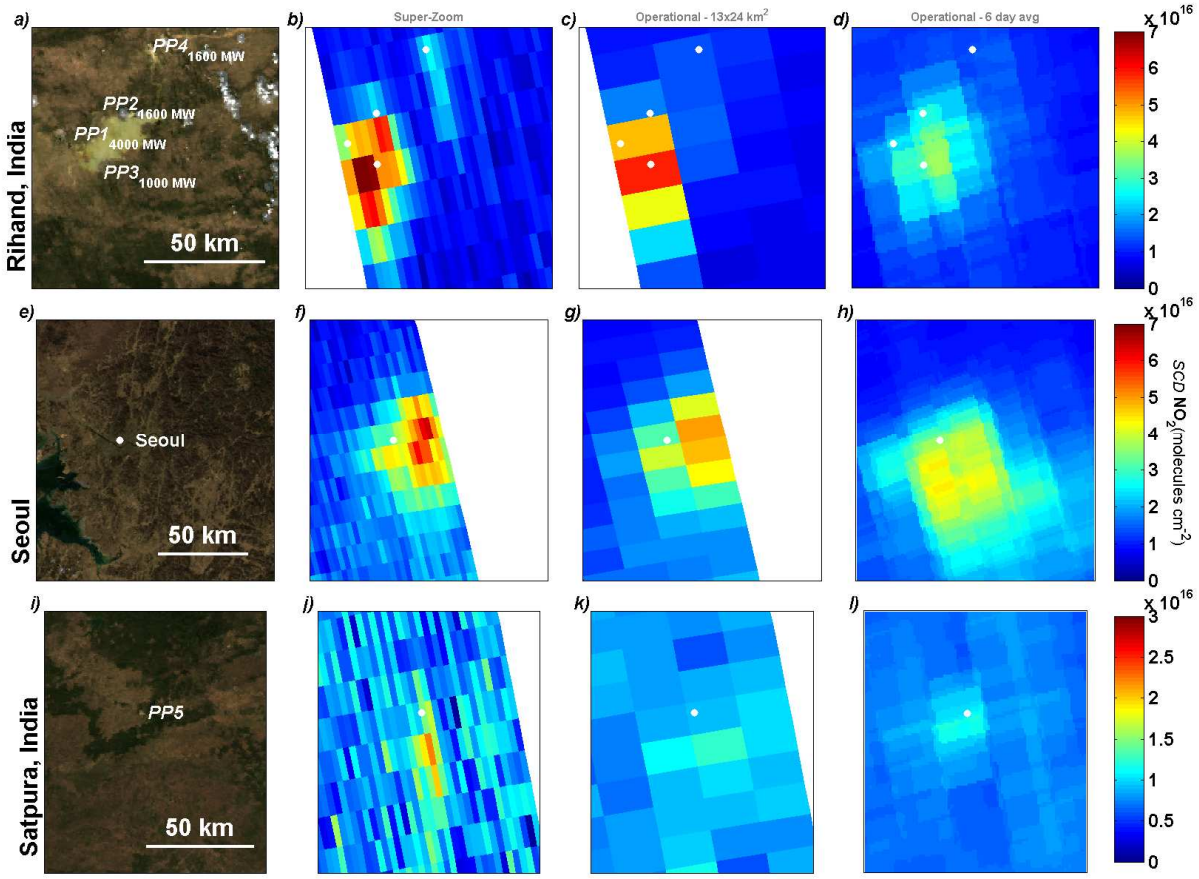

Figure 2.3 MODIS RGB image, slant column NO_2 retrieved from OMI super-zoom and operational resolution observations and from six operational resolution observations over the Rihand Reservoir in India (a–d), Seoul, South Korea (e–h), and Sarni, India (i–l). Power plants located around the Rihand Reservoir include Singrauli and Vindhyachal (PP1 – 4200 MW), Anpara and Hindalco (PP2 – 2400 MW), Rihand (PP3 – 1000MW pre-2006), and Obra (PP4 – 1600 MW). Power plants around Sarni, India (i), include Satpura generating station (PP5).

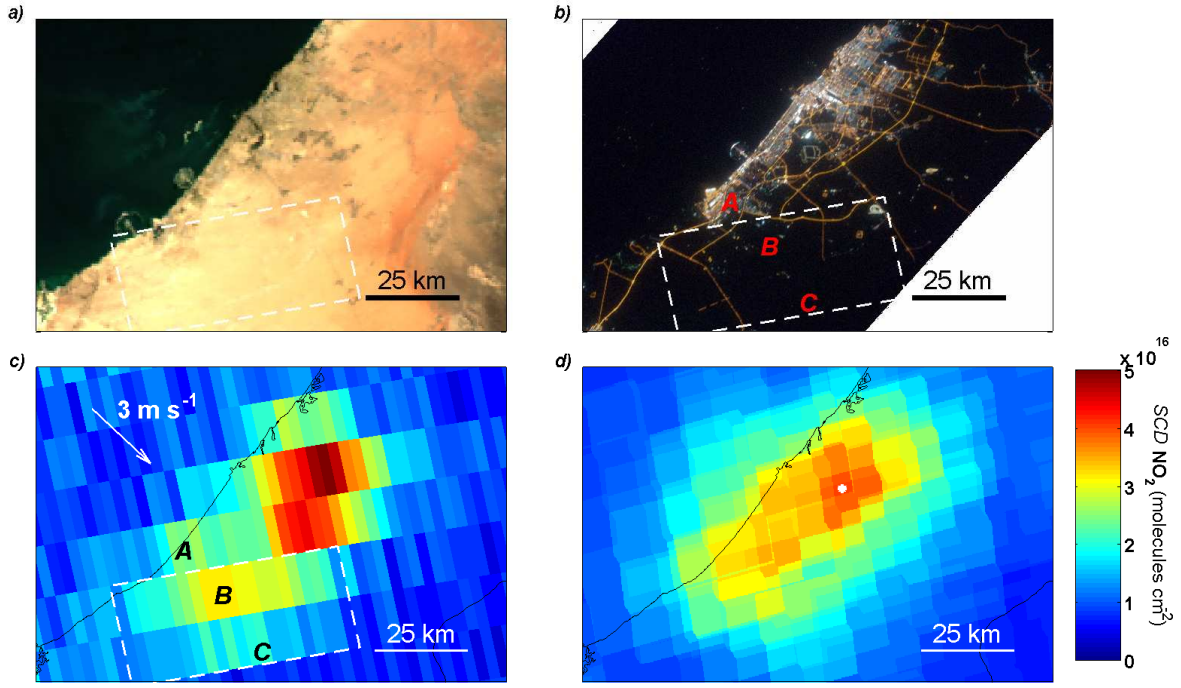

Figure 2.4 (a) True color image from Aqua-MODIS on 21 November 2004. (b) Nighttime image (courtesy of the Image Science and Analysis Laboratory, NASA Johnson Space Center, ISS020-E-39932) captured aboard the International Space Station over Dubai, UAE, on 11 September 2009 at 02:00 a.m. LST. (c) Slant column NO_2 retrieved from a single overpass on 21 November 2004 for individual pixels and (d) a six-orbit, area-weighted average of slant column NO_2 retrieved from six operational-scale orbits (Table 1). Panels (a) and (b) highlight the locations of the Jebel Ali Free Zone and a point on the downwind transect. The white arrow in (c) indicates the direction and magnitude of winds observed at the Sharjah and Dubai International Airports at midday on 21 November 2004 (NOAA NCDC DS3505).

Chapter 3 – Effects of model resolution on the interpretation of satellite NO_2 observations

3.1 Introduction

NO_x ($NO + NO_2$) is emitted to the troposphere by fossil-fuel combustion, biomass burning, soil microbial processes, and lightning. In the troposphere, NO_x affects ozone production, aerosol formation and atmospheric composition (e.g. CH_4) through feedback on HO_x ($OH + HO_2 + RO_2$). The concentration of OH radical, the main daytime sink of NO_x, depends strongly on NO_x concentration. As a result, the removal rate of NO_x (i.e. $k_{NO2+OH}[OH]$) depends strongly on its own concentration. Thus, to accurately quantify this removal rate, a model must accurately resolve NO_x from its source (10–100 ppb) to background (10-100 ppt). Column NO_2 (e.g., Heue et al., 2008; Valin et al., 2011) and in situ observations (e.g., Ryerson et al., 2001; Russell et al., 2011) show that this transition can occur at scales as small as 10–20 km, a length scale similar to those reported from calculations (e.g., Cohan et al., 2006; Loughner et al., 2007).

Satellite-based observations of tropospheric NO_2 have provided unique insights into spatial and temporal patterns on regional scales of soil (e.g., Bertram et al., 2005; van der A et al., 2007; Hudman et al., 2010), biomass burning (e.g., Jaegle et al., 2005; Mebust et al., 2011), lightning (e.g., Beirle et al., 2010), and urban NO_x emissions (e.g., Kim et al., 2009; Russell et al., 2010; Beirle et al., 2011). These satellite observations have also provided constraints on inverse models that are used to validate emission inventories (e.g., Martin et al., 2003; Konovalov et al., 2006; Napelenok et al., 2008; Kim et al., 2009). Most of the inverse modeling studies used to validate these emission inventories adjust NO_x emissions with the assumption that model chemistry is accurate. However, errors in our understanding of atmospheric reactions (e.g., Thornton et al., 2002; Mollner et al., 2010) or their representation in models may compromise the accuracy of these inferred emissions. For example, extensive research has demonstrated that modeled ozone production depends strongly on model resolution due to its nonlinear dependence on NO_x concentration (e.g., Sillman et al., 1990; Kumar et al., 1994; Gillani et al., 1996; Cohan et al., 2006; Wild and Prather, 2006). OH, which has the same NO_x-dependence as ozone production, will also vary with model resolution affecting NO_x lifetime and concentration. As a result, NO_x emissions derived from an inversion of satellite NO_2 observations will have resolution-dependent biases, the magnitude of which is not well known.

I investigate the biases in predicted NO_2 column due to model horizontal resolution. To illustrate the mechanisms at work, I first show how model resolution, OH, and NO_2 interact in 1-D and 2-D plume models. I then use WRF-Chem, a fully-coupled regional 3-D chemical transport model (CTM), to evaluate the effect in some realistic model situations. I use the simpler models to understand the source of resolution-dependent biases and use WRF-Chem to determine the model resolution necessary to predict 10 AM and 1 PM column NO_2 to 10 % and 25 % accuracy over the Four Corners and San Juan power plants, the city of Los Angeles, and the San Joaquin Valley in California for a week-long simulation in July 2006.

3.2 NO_x-OH steady-state chemistry in 1-D and 2-D plume models

Using the analytical solution to the NO_x-HO_x steady-state relationship to determine OH concentration (Table 3.1) (Murphy et al., 2006 and references therein), I simulate the removal of NO_2 by OH in the outflow of sources using both 1-D and 2-D plume models. The selected chemical parameters are representative of noontime, mid-latitude, NO_x-CH_4-CO chemistry. Figure 3.1 shows the dependence of OH on NO_2 derived from this steady-state relationship with the corresponding NO_2 lifetime indicated on the right axis $(k_{NO2+OH} \times OH)^{-1}$. As is well-known,

the response of OH to changes in NO_2 depends on NO_2 concentration. For example, decreasing NO_2 at high NO_2 (red) results in an increase of OH and a shorter NO_2 lifetime while at low NO_2 (blue), results in less OH and a longer NO_2 lifetime.

The key feature of this relationship is that the maximum in OH feedback (green) corresponds to a NO_2 lifetime of two hours, an e-folding decay length of 54 km in 5 m s^{-1} winds and of 5–15 km at the slower moving diffusive edges of a plume. Poorly resolving these gradients in NO_2 will result in inaccurate OH feedback, biases in the NO_2 lifetime, and as a result, modest biases in domain-total NO_2. For resolutions that grossly misrepresent the distribution of NO_2, biases in OH feedback, NO_2 lifetime, and domain-total NO_2 will be massive.

3.2a Biases in a 1-D plume model

In a 1-D model, NO_2 is emitted at the western end of the domain (x = 0–1024 km) and transported to the east at a constant rate (5 m s^{-1}). I run the model with emission rates of 30, 6.0, and 0.30 kmol h^{-1}. These emission rates are selected to correspond with high, intermediate and low NO_2-OH feedback regimes depicted in Figure 3.1. The model is run at east-west resolutions of 0.5 km to 512 km with the dimensions perpendicular to the flow fixed at 1 km (north-south and vertical).

When 1-D simulations are run to steady-state, NO_2 is removed by OH such that the spatial gradient reflects the applied NO_2-OH feedback (Fig. 3.2). Failure to accurately resolve these gradients results in inaccurate OH and biases in both the NO_2 lifetime and concentration. For example, when a large source of NO_2 is computed at 2 km resolution, OH is suppressed so strongly that NO_2 decays by only one e-fold in 400 km, corresponding to a chemical lifetime of 22 h (Fig. 3.2 a, d – solid line). Computed at coarser resolution (128 km), NO_2 is averaged over the entire grid cell such that OH is enhanced, NO_2 is shorter-lived, and NO_2 concentrations are biased low (Fig. 3.2 a, d – dashed line). At this high emission rate, biases in the domain-total NO_2 exceed 50 % at the coarsest resolutions (Fig. 3.3).

In contrast to a large source, NO_2 emitted from a small source decays rapidly when computed at 2 km resolution, a reflection of high OH concentration (Fig. 3.2 c, f – solid line), but at coarser model resolution (128 km), NO_2 is instantaneously mixed over an entire grid cell resulting in lower OH, a longer NO_2 lifetime, and a corresponding positive bias in domain-total NO_2 concentration (Fig. 3.2 c, f – dashed line, Fig. 3.3).

For an intermediate source of NO_2, the plume decays by an e-fold within 60 km at 2 km model resolution, a gradient corresponding to a chemical lifetime of about three hours and near-maximum OH (Fig. 3.2 b, e – solid line). Model calculations at coarser resolutions (128 km) are not capable of resolving this sharp gradient. Because NO_2 concentrations predicted for an intermediate source are near the maximum OH (Fig. 3.1), biases behave like those of a large source at finer model resolutions and like those of a small source at coarser resolutions (Fig. 3.3).

In a 1-D model, domain-averaged NO_2 predicted at coarse resolutions is biased (Fig. 3.3). At intermediate resolutions the biases are moderate (10–30 %) and result from numerical resolution that dilute NO_2 at the leading edge of the plume and shift OH to the left in Figure 3.1. When the model resolution becomes much larger than the plume itself, OH feedbacks are shifted by a factor 2-5 times that of the plume simulated in a resolved calculation (e.g., Fig. 3.2 a, d) and gross biases in domain-total NO_2 are predicted (>50 %, Fig. 3.3).

3.2b Biases in a 2-D plume model

While 1-D models are illustrative, 2-D models are a better approximation of NO_2 column and provide some additional insights. For instance, I can consider the effects of horizontal diffusion as well as different source distributions. In this 2-D model, I define a point source (2×2 km^2) with emission rates of 200, 40, and 2 kmol h^{-1} and an area source (96×96 km^2) with emission rates of 1000, 200, and 10 kmol h^{-1} both located in the far southwest corner ($x = y = 0$ km) of the domain ($x = y = 0$–384 km). These emission rates are selected so that the simulated plume concentration corresponds with the high, intermediate and low NO_2-OH feedback regimes depicted in Figure 3.1. In this model, NO_2 is transported with x and y wind speeds of 3 m s^{-1}, a mean flow of $3\sqrt{2}$ m s^{-1} to the northeast. Diffusion rates are set to 10 m^2 s^{-1}. Initial and horizontal boundary concentrations are set to 0.5 ppt. The model is computed at six grid resolutions (2, 4, 12, 24, 48, and 96 km), with the vertical layer fixed at 1 km. I run simulations of NO_2 with OH determined by the steady state equation (Table 3.1, Fig. 3.1).

When the 2-D model is run to steady-state, a large point source of NO_2 is OH suppressing and long-lived when simulated at 2 km model resolution, but experiences high OH and is short-lived when simulated at coarse resolution (96 km) (Fig. 3.4, a–c). Because the resolved plume is so narrow (~$24\sqrt{2}$ km, Fig. 3.4a), the distribution of NO_2 and the corresponding OH feedbacks are grossly misrepresented at 96 km resolution with biases in domain-averaged NO_2 as high as 75 % (Fig. 3.5b). Over a small source (not shown), the opposite effect occurs in a model; a small source is OH-enhancing and short-lived at 2 km resolution, but experiences low OH and is long-lived at coarser resolutions. As a result, domain-averaged NO_2 predicted over a small source is biased 100 %.

When the same 2-D model is run to steady-state using emissions from an area source (Fig. 3.4, d–f), domain-averaged biases in NO_2 are relatively modest (~25 % at 96 km model resolution) but follow the same general pattern as those simulated over a point source (Fig. 3.5). The biases predicted over an area source are smaller because coarse model resolutions are better able to characterize the distribution of NO_2 and corresponding OH feedbacks over the simulated plume, which is much wider than that predicted over a point source. From previous discussion, it would be expected that simulation of NO_2 at 96 km model resolution would be massively biased since the resolved plume is approximately 96 km wide. However, the alignment of this area source (96×96 km^2) on this 96-km grid results in an NO_2 distribution that roughly approximates that simulated in a resolved model, resulting in biases that are relatively small (~25 %). When the 96×96 km^2 area source is shifted by 48 km and evenly distributed over four 96 km grid cells (not shown), biases predicted at 96 km resolution are as large as those predicted for a point source (> 75 %).

Figure 3.5 summarizes biases predicted in a 2-D model as a function of model resolution, source strength, and proximity to the source. Biases predicted for NO_2 in a constant OH field (OH = 5.5×10^6 molecules cm^{-3}), that is without any NO_2-OH feedback and only subject to transport effects (Fig. 3.5, b–e, black line), are negligible over the entire domain (~0 %, 3.5b), significant over the 192 km nearest the source (−10 %, 3.5c), and large in both the 96 km nearest the source (−30 %, 3.5d) and in a 12×12 km^2 pixel 96 km downwind from the source (−75 %, 3.5e). Without OH feedback, these biases are due to numerical artifacts in computing a short-lived species on a coarse grid, but are negligible over regions that are large (e.g., 192 km) compared to the spatial scale of chemical decay (e-fold decay over 84 km) (e.g., Fig. 3.5c, black). When subject to NO_2-OH chemical feedbacks (Fig. 3.5, b–e, red, green, and blue lines),

biases diverge from that of transport alone (black) with behavior depending, as expected, on the rate of NO_x emissions. Over each spatial domain considered, simulation of a large source (red) is biased low versus transport alone (black) whereas the opposite is true for a small source (blue). For both large and small sources, the magnitude of the bias increases as the model resolution coarsens. In both the point and area source examples, the behavior of biases depends on model resolution. VOC reactivity affects predicted biases by altering the NO_2 concentration at which maximum OH occurs (Fig. 3.1, Table 3.1). For simulations with VOC reactivity increased by a factor of 10 and the same NO_2 emissions, I find that the pattern of predicted biases changes in the direction one expects based on the shifts in the NO_2-OH relationship for an increase in VOC. However, if the NO_x emission rates are increased along with VOC reactivity, the patterns of biases returns to those predicted at the original VOC conditions.

Biases in a 2-D model are predicted to be unacceptably large (up to ~75–100 %) at relevant horizontal resolutions (96 km) with behavior that depends dramatically on source strength (+100 % for small source to −75 % for large source) and distribution (~ 75 % for point source to ~ 25-75 % for area source). Biases predicted in a 2-D model are much larger than those predicted at the same model resolution in a 1-D model because the plume can diffuse horizontally. However, the basic resolution dependent effects are the same – numerical dilution shifts the NO_x-OH feedback to the left on Figure 3.1, altering the spatial pattern of NO_2 from a resolved calculation. These effects are modest (0–30 %) if the model resolution is finer than the width of a fully-resolved plume, but are massive (>50 %) if the resolution is comparable to or larger than the plume (Figs. 3.4, 3.5).

3.3 Effects in WRF-Chem over Four Corners, Los Angeles, and San Joaquin Valley

Regional CTMs, like WRF-Chem (Grell et al., 2005), provide a realistic and fully-coupled description of atmospheric mixing, chemistry, and emissions. I use WRF-Chem to test for resolution-dependent biases over three distinct source regions: the Four Corners Power Plants, Los Angeles, and the San Joaquin Valley. Air quality control strategies often use 10 or 25 % NO_x reductions as a realistic regulatory benchmark. Using WRF-Chem, I simulate the 10 AM and 1 PM NO_2 column, as would be observed by space-based UV/VIS instruments, over the Four Corners and San Juan Power Plants in Northwest New Mexico (185 kmol h^{-1}) at 1, 4, 12, and 24 km resolution and over California, which includes the Los Angeles Basin (1020 kmol h^{-1}) and the San Joaquin Valley (410 kmol h^{-1}) at 4, 12, 24, 48, and 96 km resolution to examine the grid resolution necessary to attain 10 % and 25 % accuracy for a 1-7 July 2006 simulation. For a more detailed description of the WRF-Chem simulations see the Appendix.

Four Corners, Los Angeles and the San Joaquin Valley are large enough sources of NO_x such that OH is suppressed in a resolved simulation. For example, effective OH, or the NO_2-weighted OH concentration that is simulated at 1 km resolution over Four Corners is low ($<5 \times 10^6$ molecules cm^{-3}) where NO_2 concentration is high (Fig. 3.6, a–b, red), enhanced ($>1.5 \times 10^7$ molecules cm^{-3}) where NO_2 is intermediate (Fig. 3.6, a-b, green) and low ($\sim 5 \times 10^6$ molecules cm^{-3}) where NO_2 is low (Fig. 3.6, a–b, blue). At coarser resolutions, NO_2 is numerically diluted, and prediction of NO_2 column is biased low just as was predicted over large sources in the 1-D and 2-D plume models. Over Four Corners, the 1 PM NO_2 column simulated at 24 km is biased −50 % relative to simulation at 1 km (Fig. 3.7). Over Los Angeles, the 1 PM NO_2 column is biased −13 % at 24 km resolution relative to simulation at 4 km, but is biased −37 % at 96 km resolution (Fig. 3.8). Over the San Joaquin Valley, the biases relative to 4 km simulation are −16 % at 12 km resolution, −24 % at 24 km resolution and −36 % at 48 km resolution (Fig. 3.9).

I find that the exact numbers depend on the choice of the boundaries that surround each plume, but that the conclusions are independent of that choice. As a result of these biases, prediction of the domain-averaged NO_2 column to 25 % accuracy at 1 PM requires model resolution of 4 km over Four Corners, 12 km over San Joaquin Valley, and 48 km over Los Angeles under the conditions tested here. For 10 % accuracy, 4 km model resolution is required over Four Corners and the San Joaquin Valley while 12 km resolution is sufficient over Los Angeles.

Biases in NO_2 column at 10 AM (not shown) are consistently smaller than those predicted at 1 PM because the NO_2 column predicted at 10 AM is exposed to much less OH through the nighttime and early morning hours. As a result, prediction of 10 AM NO_2 column to 25 % accuracy as tested here requires slightly coarser model resolution than was necessary at 1 PM: 12 km over Four Corners, 24 km over San Joaquin Valley, and 48 km over Los Angeles. For 10 % accuracy, model resolution of 4 km is necessary over Four Corners, 24 km over San Joaquin Valley and 48 km over Los Angeles.

All three of these regions are biased low at coarse model resolutions (Figs. 3.7–3.9), which is expected for large, OH-suppressing sources of NO_x. For Los Angeles and Four Corners, sources that are comparable to the large 2-D area and point sources tested in the plume model, biases behave similarly to those predicted in the 2-D plume model. And while the San Joaquin Valley appears to be an intermediate source of NO_x (Fig. 3.9), which according to the 2-D plume model would indicate that coarse resolution prediction of NO_2 should be biased high (Fig. 3.5h), it is important to consider the differences between the 2-D plume model, which simulates midday summertime chemistry at steady-state, with WRF-Chem, which integrates the full diurnal cycle. In WRF-Chem, all of these sources (Figs. 3.7–3.9), including the San Joaquin Valley, suppress OH through the morning hours when NO_x concentrations are higher and HO_x production rate is lower, leading to biases that start small in the morning hours and grow with time of day.

3.4 Implications for interpretation of satellite observations

The calculations above show that predicted NO_2 columns will depend on the resolution of the model. As a consequence, any inference of NO_x emissions that relies on a model to interpret satellite observations will have biases if the model resolution is too coarse. The calculations above show that the biases are both positive and negative as a result of the interplay of NO_2 and OH. I find that predicted biases are especially large where steep gradients of NO_2 dominate the total NO_2 mass (e.g. 2-D point source) and that they are smaller where shallow gradients dominate the total NO_2 mass (e.g. 2-D area source). In general, gradients are shallow where NO_x lifetime is long compared to transport timescales (e.g. wintertime, morning hours) and are steep where NO_x lifetime is short compared to the timescale of transport (e.g. summertime, afternoon hours).

For situations presented here, model resolution in the range of 4–12 km is sufficient to predict the effects of NO_2-OH feedbacks on the NO_2 lifetime and column to 10 % accuracy. This value will change depending on the location, season, and time of day according to general guidelines provided above. Nonetheless my analysis suggests that numerical resolution needs to be small compared to the NO_x e-folding distance. A growing set of observations over both power plants and urban sources at different times of year indicate that boundary layer NO_x often exhibit e-folding distances of order 10 km – 30 km (e.g., Ryerson et al., 2001; Loughner et al., 2007; Heue et al., 2008; Russell et al., 2011; Valin et al., 2011) supporting the idea that model

resolution in the range of 4-12 km is necessary in a broad range of contexts. For any calculation where accurate computation of boundary layer NO_x is important I recommend model calculations to test whether the spatial resolution is sufficient to calculate NO_2 to the desired accuracy.

3.5 Conclusions

I investigate the effects of NO_2-OH chemical feedbacks on predicted NO_2 in a 1-D plume model, a 2-D plume model, and WRF-Chem, a fully-coupled 3-D CTM. I use 1-D and 2-D plume models to demonstrate that nonlinear NO_2-OH chemical feedback leads to biases in column NO_2. As a result, inference of NO_x emission inventories from chemical transport models will suffer biases that depend on the horizontal resolution of the model. Using WRF-Chem, I determine the model resolution necessary to predict NO_2 column to 10 % and 25 % accuracy over Los Angeles, the San Joaquin Valley, and Four Corners for a week-long simulation in July 2006. In this example, I find that prediction of NO_2 column to 10 % accuracy at 1 PM requires model resolution of 4 km over both Four Corners and the San Joaquin Valley while 12 km is sufficient over Los Angeles. Prediction to 10 % accuracy at 10 AM requires model resolution of 4 km over Four Corners, 24 km over San Joaquin Valley, and 48 km over Los Angeles. In these examples, I find that model resolution must be comparable to, or smaller than, the spatial variability of NO_2 to accurately model NO_2-OH feedbacks on NO_2 column. Thus, simulations aimed at matching satellite observations must be run at sufficient spatial resolution to avoid contamination by numerical artifacts.

Appendix – 3.A

I simulate column NO_2 from 1–7 July 2006, over California, Nevada, Northern Mexico, and the Eastern Pacific centered over Southern California (2304 × 2304 km^2) at 4, 12, 24, 48, and 96 km resolution. The simulated domain is much larger than the region of interest to ensure that there are no effects of boundary conditions in the coarser resolution model simulations. The first two days of simulation are used as spin-up, and the last five days (3–7 July) are averaged to 1 p.m. LST for all analyses. Emissions are the National Emission Inventory (NEI) 2005 on-road and off-road transportation emissions for a typical July weekday and Continuous Emissions Monitoring (CEMS) averaged point source emissions for a typical August, 2006, weekday. For more information, see ftp://aftp.fsl.noaa.gov/divisions/taq/emissions data 2005/Weekday emissions/readme.txt. Biogenic emissions for all model resolutions were generated by an online module as in (Grell et al., 2005) at 4 km horizontal resolution for a single July day and kept constant throughout the 7-day simulation. I use the Regional Acid Deposition Model, version 2 chemical mechanism (Stockwell et al., 1990). The initial and boundary chemical conditions are derived from idealized profiles that are standard in WRF-Chem. Radiative feedback from clouds on photolysis rates was disabled in order to simulate column NO_2 under clear-sky conditions that are typical of satellite observations. Meteorological initial and boundary conditions for the simulation are derived from the North American Regional Reanalysis for July 2005 (NARR – http://nomads.ncdc.noaa.gov/dods/ NCEP NARR DAILY).

I simulate column NO_2 over the Four Corners region in the Western US (384 × 384 km^2) at 1 km, 4 km, and 12 km resolution and extend the boundaries (1536 × 1536 km^2) to simulate the same domain at 24 km resolution. This domain is centered on the Four Corners and San Juan Power Plants, which are approximately 20 km apart. This simulation is run in the same manner as that run over California except that only emissions from point sources are included. For

simulation at 24 km resolution, as mentioned, the domain is extended to avoid boundary relaxation effects that occur over the 5 boundary grid cells in WRF-Chem.

References

Beirle, S., Huntrieser, H., and Wagner, T.: Direct satellite observation of lightning-produced NO_x, Atmospheric Chemistry and Physics, 10, 10965-10986, 2010.

Beirle, S., Boersma, K. F., Platt, U., Lawrence, M. G., and Wagner, T.: Megacity Emissions and Lifetimes of Nitrogen Oxides Probed from Space, Science, 333, 1737-1739, 2011.

Bertram, T. H., Heckel, A., Richter, A., Burrows, J. P., and Cohen, R. C.: Satellite measurements of daily variations in soil NO_x emissions, Geophysical Research Letters, 32, L24812, 2005.

Cohan, D. S., Hu, Y. T., and Russell, A. G.: Dependence of ozone sensitivity analysis on grid resolution, Atmospheric Environment, 40, 126-135, 2006.

Gillani, N. V., and Pleim, J. E.: Sub-grid-scale features of anthropogenic emissions of NO_x and VOC in the context of regional Eulerian models, Atmospheric Environment, 30, 2043-2059, 1996.

Grell, G. A., Peckham, S. E., Schmitz, R., McKeen, S. A., Frost, G., Skamarock, W. C., and Eder, B.: Fully coupled "online" chemistry within the WRF model, Atmospheric Environment, 39, 6957-6975, 2005.

Heue, K. P., Wagner, T., Broccardo, S. P., Walter, D., Piketh, S. J., Ross, K. E., Beirle, S., and Platt, U.: Direct observation of two dimensional trace gas distributions with an airborne Imaging DOAS instrument, Atmospheric Chemistry and Physics, 8, 6707-6717, 2008.

Hudman, R. C., Russell, A. R., Valin, L. C., and Cohen, R. C.: Interannual variability in soil nitric oxide emissions over the United States as viewed from space, Atmospheric Chemistry and Physics, 10, 9943-9952, 2010.

Jaegle, L., Steinberger, L., Martin, R. V., and Chance, K.: Global partitioning of NO_x sources using satellite observations: Relative roles of fossil fuel combustion, biomass burning and soil emissions, Faraday Discussions, 130, 407-423, 2005.

Kim, S. W., Heckel, A., Frost, G. J., Richter, A., Gleason, J., Burrows, J. P., McKeen, S., Hsie, E. Y., Granier, C., and Trainer, M.: NO_2 columns in the western United States observed from space and simulated by a regional chemistry model and their implications for NO_x emissions, Journal of Geophysical Research-Atmospheres, 114, 29, D11301, 2009.

Konovalov, I. B., Beekmann, M., Richter, A., and Burrows, J. P.: Inverse modelling of the spatial distribution of NO_x emissions on a continental scale using satellite data, Atmospheric Chemistry and Physics, 6, 1747-1770, 2006.

Kumar, N., Odman, M. T., and Russell, A. G.: Multiscale air quality modeling: Application to southern California, Journal of Geophysical Research-Atmospheres, 99, 5385-5397, 1994.

Loughner, C. P., Lary, D. J., Sparling, L. C., Cohen, R. C., DeCola, P., and Stockwell, W. R.: A method to determine the spatial resolution required to observe air quality from space, Ieee Transactions on Geoscience and Remote Sensing, 45, 1308-1314, 2007.

Martin, R. V., Jacob, D. J., Chance, K., Kurosu, T. P., Palmer, P. I., and Evans, M. J.: Global inventory of nitrogen oxide emissions constrained by space-based observations of NO_2 columns, Journal of Geophysical Research-Atmospheres, 108, 4537, 2003.

Mebust, A. K., Russell, A. R., Hudman, R. C., Valin, L. C., and Cohen, R. C.: Characterization of wildfire NO_x emissions using MODIS fire radiative power and OMI tropospheric NO_2 columns, Atmospheric Chemistry and Physics, 11, 5839-5851, 2011.

Mollner, A. K., Valluvadasan, S., Feng, L., Sprague, M. K., Okumura, M., Milligan, D. B., Bloss, W. J., Sander, S. P., Martien, P. T., Harley, R. A., McCoy, A. B., and Carter, W. P. L.: Rate of Gas Phase Association of Hydroxyl Radical and Nitrogen Dioxide, Science, 330, 646-649, 2010.

Murphy, J. G., Day, D. A., Cleary, P. A., Wooldridge, P. J., Millet, D. B., Goldstein, A. H., and Cohen, R. C.: The weekend effect within and downwind of Sacramento: Part 2. Observational evidence for chemical and dynamical contributions, Atmospheric Chemistry and Physics Discussions, 6, 11971-12019, 2006.

Napelenok, S. L., Pinder, R. W., Gilliland, A. B., and Martin, R. V.: A method for evaluating spatially-resolved NO_x emissions using Kalman filter inversion, direct sensitivities, and space-based NO_2 observations, Atmospheric Chemistry and Physics, 8, 5603-5614, 2008.

Russell, A. R., Valin, L. C., Bucsela, E. J., Wenig, M. O., and Cohen, R. C.: Space-based Constraints on Spatial and Temporal Patterns of NO_x Emissions in California, 2005-2008, Environmental Science & Technology, 44, 3608-3615, 2010.

Russell, A. R., Perring, A. E., Valin, L. C., Bucsela, E. J., Browne, E. C., Min, K. E., Wooldridge, P. J., and Cohen, R. C.: A high spatial resolution retrieval of NO_2 column densities from OMI: method and evaluation, Atmospheric Chemistry and Physics, 11, 8543-8554, 2011.

Ryerson, T. B., Trainer, M., Holloway, J. S., Parrish, D. D., Huey, L. G., Sueper, D. T., Frost, G. J., Donnelly, S. G., Schauffler, S., Atlas, E. L., Kuster, W. C., Goldan, P. D., Hubler, G., Meagher, J. F., and Fehsenfeld, F. C.: Observations of ozone formation in power plant plumes and implications for ozone control strategies, Science, 292, 719-723, 2001.

Sillman, S., Logan, J. A., and Wofsy, S. C.: A regional scale model for ozone in the United States with subgrid representation of urban and power plant plumes, Journal of Geophysical Research-Atmospheres, 95, 5731-5748, 1990.

Stockwell, W. R., Middleton, P., Chang, J. S., and Tang, X. Y.: The 2nd generation Regional Acid Depostion Model chemical mechanism for regiona air quality modeling, Journal of Geophysical Research-Atmospheres, 95, 16343-16367, 1990.

Thornton, J. A., Wooldridge, P. J., Cohen, R. C., Martinez, M., Harder, H., Brune, W. H., Williams, E. J., Roberts, J. M., Fehsenfeld, F. C., Hall, S. R., Shetter, R. E., Wert, B. P., and Fried, A.: Ozone production rates as a function of NO_x abundances and HO_x production rates in the Nashville urban plume, Journal of Geophysical Research-Atmospheres, 107, 4146, 2002.

Valin, L., Russell, A., Bucsela, E., Veefkind, J., and Cohen, R.: Observation of slant column NO_2 using the super-zoom mode of AURA-OMI, Atmospheric Measurement Techniques, 4, 1929-1935, 2011.

van der A, R. J., Eskes, H. J., Boersma, K. F., van Noije, T. P. C., Van Roozendael, M., De Smedt, I., Peters, D., and Meijer, E. W.: Trends, seasonal variability and dominant NO_x source derived from a ten year record of NO_2 measured from space, Journal of Geophysical Research-Atmospheres, 113, D04302, 2008.

Wild, O., and Prather, M. J.: Global tropospheric ozone modeling: Quantifying errors due to grid resolution, Journal of Geophysical Research-Atmospheres, 111, D11305, 2006.

Table 3.1 Parameters used in HO_x-NO_x steady-state model (Murphy et. al., 2006 and references therein).

Parameter	Value
Initiation	
HO_x Production	0.5×10^7 molecules cm^{-3} s^{-1}
Radical Chain Propagation	
$k_{OH+VOC}[VOC]$	$1\ s^{-1}$
$k_{RO2+NO \rightarrow RO+NO2}$	8×10^{-12} cm^3 molecules^{-1} s^{-1}
Termination	
$k_{RO2+RO2-Eff}$	7.5×10^{-12} cm^3 molecules^{-1} s^{-1}
k_{NO2+OH}	1×10^{-11} cm^3 molecules^{-1} s^{-1}
$k^a_{RO2+NO \rightarrow RONO2}$	0 cm^3 molecules^{-1} s^{-1}
$NO_2 : NO_x$	0.7

[a]Alkyl-nitrate formation rate has been set to 0 in these simulations. Increases in this rate will slightly affect NO_x lifetime.

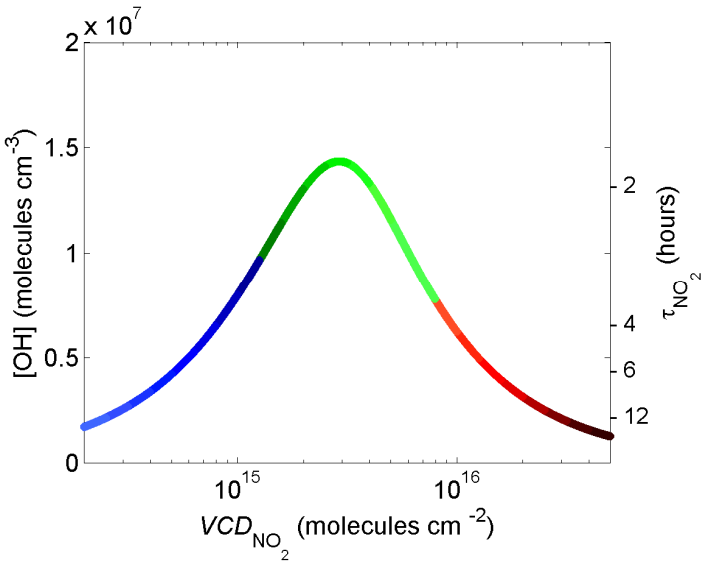

Figure 3.1 Steady state OH concentration (left axis) and corresponding NO_2 lifetime $(k_{NO2+OH} \times OH)^{-1}$ on the right axis versus boundary layer NO_2 column (molecules cm^{-2}) assuming a 1 km well-mixed boundary layer. The color scheme corresponds to regions of high NO_2 (red) where OH is low, intermediate NO_2 (green) where OH is high, and low NO_2 (blue) where OH is low. This color scheme is used throughout this chapter.

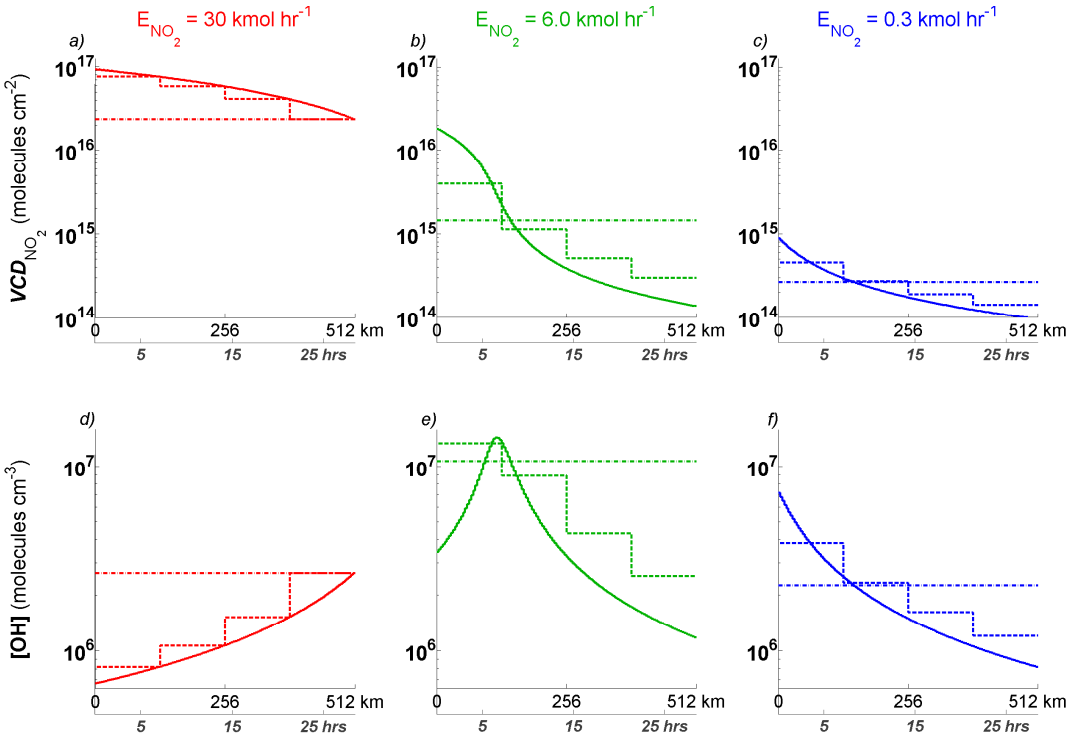

Figure 3.2 NO_2 column (molecules cm^{-2}) predicted in a 1-D plume model at 2 km (solid), 128 km (dashed), and 512 km model resolutions (dash-dot) for (a) a large, (b) intermediate, and (c) small source of NO_2 and (d–f) the corresponding OH feedback. The color-scheme corresponds to NO_2-OH feedback regimes depicted in Figure 1. Horizontal (N–S) and vertical layers are fixed at 1 km thickness for all resolutions.

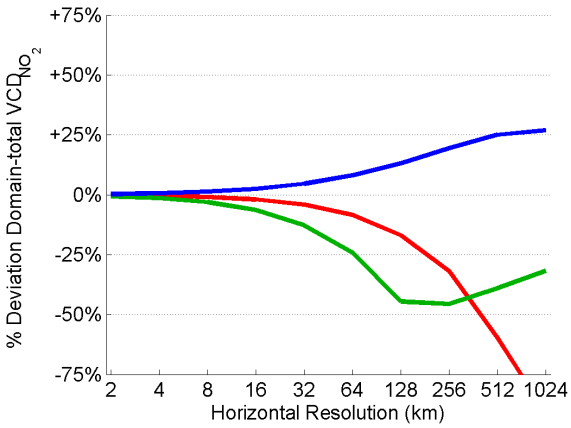

Figure 3.3 Resolution-dependent bias in domain-averaged NO_2 column versus model resolution for small (blue), intermediate (green), and large (red) sources of NO_2 in a 1-D plume model (Fig. 2).

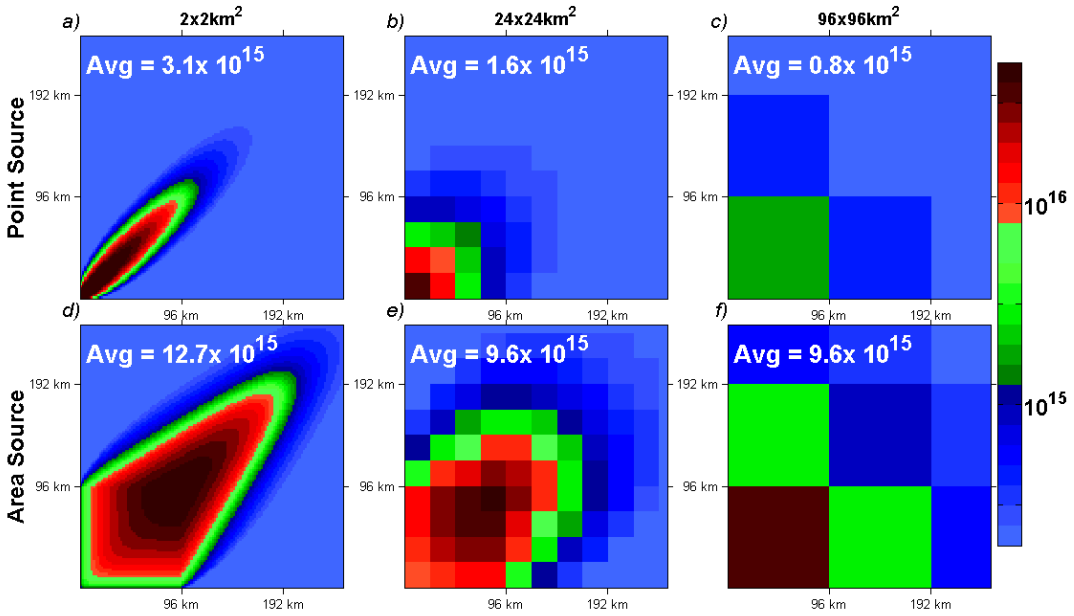

Figure 3.4 NO_2 column (molecules cm^{-2}) predicted in a 2-D plume model for a large point source simulated at (a) 2 km, (b) 24 km, and (c) 96 km resolution, and the same for simulation of a large area source (d–f). The color-scheme corresponds to NO_2-OH feedback regimes depicted in Figure 1. The vertical layer is fixed at 1 km thickness for all simulations shown.

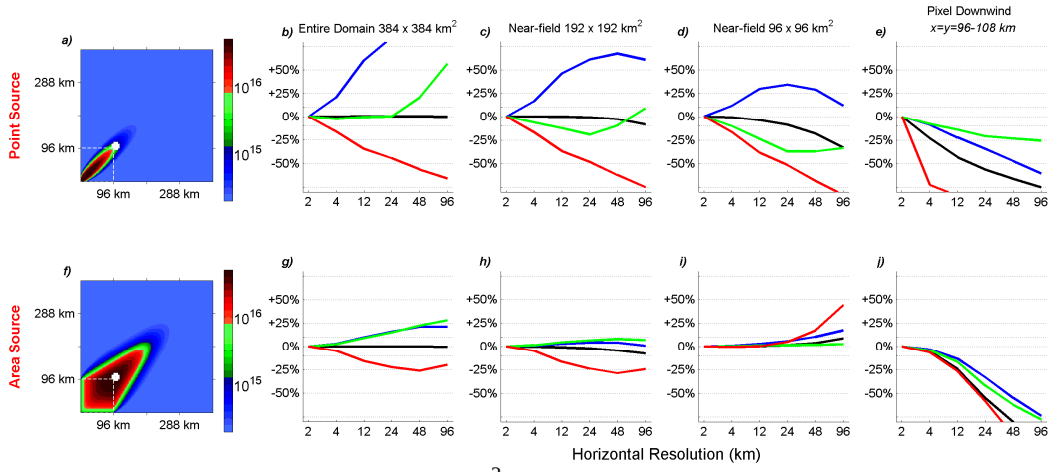

Figure 3.5 (a) NO_2 column (molecules cm^{-2}) predicted in a 2-D plume model for a large point source simulated at 2 km resolution with vertical layer fixed at 1 km thickness. Resolution-dependent bias in domain-averaged NO_2 column over the (b) entire domain (x =y =0–384 km), (c) the 192 km near-field (x =y =0–192 km), (d) the 96 km near-field (x =y =0–96 km), and (e) at a pixel downwind (x =y =96–108 km) for NO_2 emitted from a large (red), an intermediate (green), and a small (blue) point source of NO_2 with OH=f_{NO2} as in Figure 1 and from a large point source with OH set to 5×10^6 molecules cm^{-3} (black). (f–j) The same for simulation of a 96×96 km^2 area source.

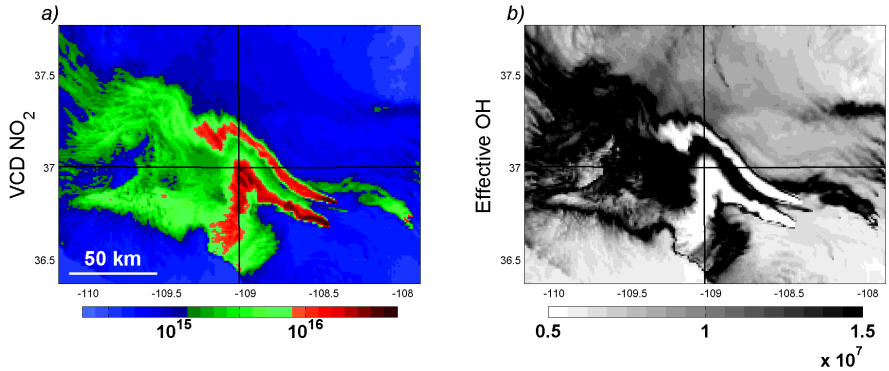

Figure 3.6 (a) NO_2 column (molecules cm^{-2}) and (b) the effective OH concentration, or the NO_2-weighted average of OH (molecule cm^{-3}), taken over the entire vertical column as simulated with WRF-Chem at 1 km resolution over the Four Corners Region of US at 10 AM on 5 July 2006.

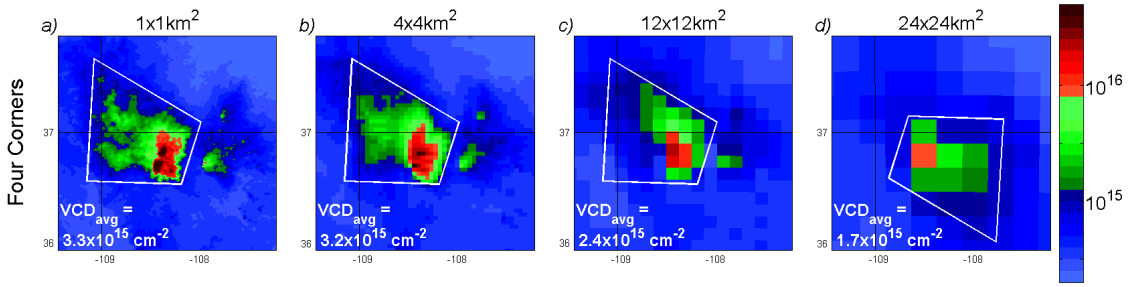

Figure 3.7 The WRF-Chem 3–7 July 2006, 1 PM LST average NO_2 column (molecules cm^{-2}) simulated over Four Corners Region of US at (a) 1 km, (b) 4 km, (c) 12 km, and (d) 24 km model resolution. NO_2 column is averaged over the sub-domain indicated by the white inset and is reported in the bottom-left corner of each panel. The sub-domain in the 24 km simulation was rotated to include the plume, which was predicted further to the SE than those predicted at 1 km, 4 km, or 12 km resolution.

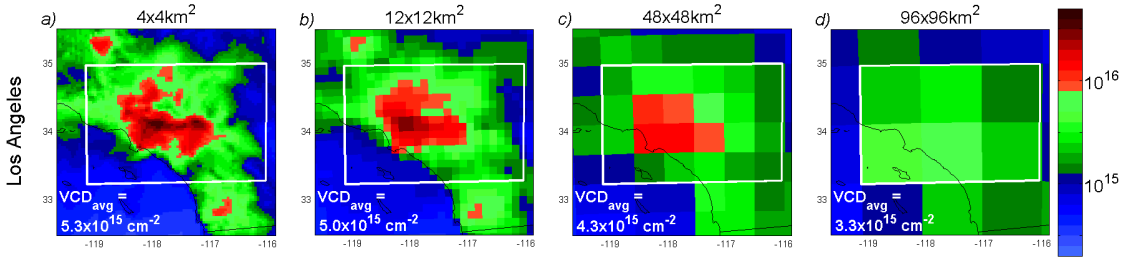

Figure 3.8 The WRF-Chem 3–7 July 2006, 1 PM LST average NO_2 column (molecules cm^{-2}) simulated over Los Angeles at (a) 4 km, (b) 12 km, (c) 48 km, and (d) 96 km model resolution. NO_2 column is averaged over the sub-domain indicated by the white inset and is reported in the bottom-left corner of each panel.

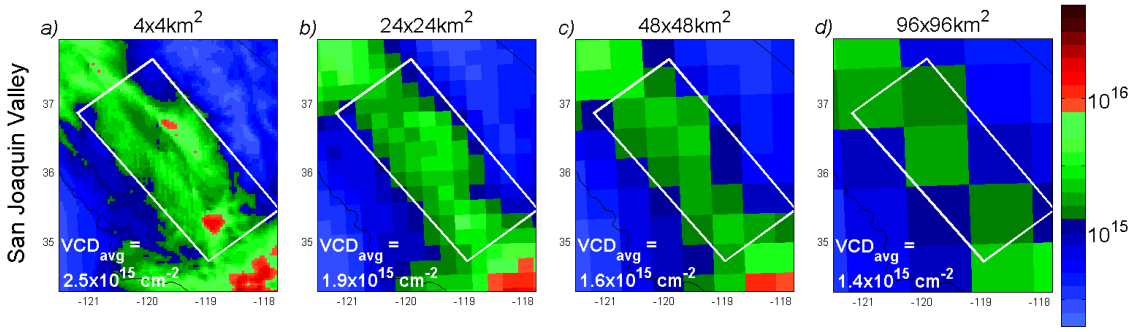

Figure 3.9 The WRF-Chem 3–7 July 2006, 1 PM LST average NO_2 column (molecules cm^{-2}) over the San Joaquin Valley at (a) 4 km, (b) 12 km, (c) 24 km, and (d) 48 km model resolution. NO_2 column is averaged over the sub-domain indicated by the white inset and is reported in the bottom-left corner of each panel.

Chapter 4 – Variations of OH radical in an urban plume inferred from NO_2 column measurements

4.1 Introduction

Nitrogen oxides ($NO_x \equiv NO + NO_2$) play a critical role in atmospheric chemistry through their effect on ozone production, particulate formation mechanisms, and atmospheric oxidation rates. NO_x is emitted by fossil fuel combustion, biomass burning, soil microbial activity and lightning and is removed by reaction of NO_2 with OH to form HNO_3, by formation of peroxyacyl nitrate (PAN), and by formation of alkyl nitrates ($RONO_2$), the production rate of the latter two depending indirectly on OH. The concentration of OH depends on the concentration of NO_x introducing a powerful nonlinear feedback of NO_x on its own lifetime (Fig. 4.1). NO_x has a relatively short lifetime in the troposphere, ranging from a few hours near the Earth's surface to weeks in the free troposphere where NO_x concentrations are typically 10's of ppt.

Observations of the NO_2 column from space have provided insight into global and regional patterns of NO_x emissions from all sources (e.g., Jaegle et al., 2005; van der A et al., 2008) and with detailed focus on individual sources such as fossil fuel use (e.g., Kim et al., 2009; Castellanos and Boersma, 2012; Russell et al., 2012), biomass burning (e.g., Mebust et al., 2011), soil microbial processes (e.g., Bertram et al., 2005; Hudman et al., 2010; Hudman et al., 2012), and lightning (e.g., Choi et al., 2005; Beirle et al., 2010; Bucsela et al., 2010). A variety of approaches to using the satellite observations to constrain emissions have been proposed (e.g., Martin et al., 2003; Stavrakou et al., 2008; Kim et al., 2009; Lamsal et al., 2011; Miyazaki et al., 2012). Most of these implicitly assume that the rate of NO_x chemical removal in the model is accurate and adjust emissions to match observed columns. Simultaneously deriving both the emission and chemical removal rate of NO_x directly from the satellite observations is difficult for a number of reasons, not the least of which is that the lifetime of NO_x is a nonlinear function of the NO_x concentration (Fig. 4.1), and consequently, also model resolution (Valin et al., 2011b). Beirle et al. (2011) developed an algorithm to evaluate the decay of the NO_2 column downwind of NO_x emission sources that allowed them to simultaneously infer the paired value of the absolute emission rate and the average OH in urban plumes. However, we show here that due to the strong nonlinear relationship of OH and NO_2 and variations of parameters affecting that relationship, the concentration of OH inferred from the *average* spatial pattern of NO_2 in a plume is not equal to the average OH concentration for the individual realizations of the same plume. This is because the average product of NO_2 and OH is not equal to the product of the average NO_2 and average OH. Furthermore, NO_2 columns are not just affected by OH, but also by the formation and the decay of PAN and $RONO_2$ molecules (e.g., Perring et al., 2010) as well as by vertical and horizontal transport.

Here, we describe a conceptual model that builds on our previous analysis of NO_2, OH and model resolution (Valin et al., 2011b) to include the effects of PAN, the NO_x steady-state, and boundary layer venting. We then investigate the functional dependence of the NO_2 column on the wind speed. We use the correlation between wind speed and the decay of NO_2 plumes to extract information on the nonlinear relationship of OH and NO_x.

4.2 Conceptual model

Figure 4.2 depicts the processes known to be important to the chemical evolution of an NO_2 plume transported within the boundary layer at a constant velocity. The figure illustrates (1) the permanent removal of NO_x by reaction of NO_2 with OH, (2) the instantaneous steady-state

relationship of NO_2 and NO_x, (3) the temporary removal and re-release of NO_x by PAN, and (4) the export of NO_x from the planetary boundary layer to the free troposphere (where the winds are in general faster and not always aligned with the boundary layer winds below them).

The permanent removal of NO_x depends on OH and OH depends on NO_x (Fig. 4.1). As a result of this feedback on its own lifetime, the spatial pattern of NO_2 column depends on the concentration of NO_x. In Valin et al. (2011b), we showed that the spatial gradients of NO_2 column downwind of a source are shallow when the concentration of NO_x is high (OH is low), steep when the concentration of NO_x is intermediate (OH is high), and shallow again when NO_x is low. The spatial dimensions of observed NO_2 gradients are shown to have e-folding distances as small as 20 km–40 km, a length scale similar to the dimensions of the nadir pixels of the OMI satellite (13×24 km^2). Consequently, it is important to take care that retrieved lifetimes are governed by physical decay of NO_2 and not an artifact of the limited spatial resolution of our measurements. This issue makes using the lower spatial resolution measurements of GOME-II or SCIAMACHY to derive OH more difficult than with OMI.

The steady-state relationship of NO_2 to NO ($\tau_{steady\text{-}state}$~100 s) affects the spatial pattern of NO_2 column in several ways. The steady-state relationship determines what fraction of NO_x (NO_2) is observable to the satellite, it determines the relative roles of NO_x loss by NO_2 and NO, and when NO_x concentrations are large compared to O_3 (e.g. in a power plant plume) it affects NO_x removal by titrating the major source of atmospheric radicals, ozone. Its effects on the spatial pattern of NO_2 column will vary with location, season, source altitude, and source type (e.g. point vs. area source).

PAN, a thermally unstable NO_x reservoir, also affects the spatial pattern of the NO_2 column. The concentration of PAN depends on the mixture and abundance of volatile organic compounds, atmospheric oxidation by OH, and temperature. It is generally thought that PAN is a sink of NO_x where the concentrations of NO_x and volatile organic compounds are high but is a source of NO_x in remote regions downwind. Thus for urban plumes formation of PAN accelerates the removal of NO_2 relative to that of OH and steepens the gradients in the near field of the source, but further downwind, releases the stored NO_2 and flattens the spatial gradient caused by reaction of NO_2 with OH.

In addition to these chemical processes, the pattern of NO_2 column also depends on atmospheric mixing. Diffusion, both vertical and horizontal, dilutes the concentration of NO_x and alters the rate of NO_x removal due to feedback on OH (Fig. 4.1). Vertical transport, or export out of the planetary boundary layer, can be thought of as a sink of NO_2 column as winds in the free troposphere are generally much faster than winds at the surface, transporting NO_x away from its source much more quickly, and the ratio of NO_2 to NO decreases as NO_x rises in to the free troposphere. The time-scale of this boundary-layer venting varies but is likely significant relative to that of chemical removal in most settings.

4.3 Results

We use observations over the city of Riyadh, Saudi Arabia, to investigate the issues outlined above. For NO_2, we use the DOMINO v2.0 retrieval of tropospheric NO_2 column (Boersma et al., 2007; Boersma et al., 2011) and for winds, the European Center for Medium-range Weather Forecast (ECMWF) ERA interim re-analysis (Dee et al., 2011); we expect that the results would be insensitive to use of alternate retrievals or wind fields. We use summertime (April-September) high-quality observations of NO_2 column (cloud fraction less than 0.20 and view-zenith angle

less than 40°). Riyadh is advantageous for this analysis because there are very few clouds in the region, providing OMI with repeated, unobstructed measurement of the full column. We experimentally determine a background column density of 9.3×10^{14} molecules cm^{-2} and subtract that value from all measurements.

Riyadh is a large, isolated source of NO_x; it has nearly 7 million inhabitants in an area of approximately 30×50 km^2 (E-W×N-S). The nearest NO_2 enhancement observed by OMI is 200 km from Riyadh (Fig. 4.3; bottom panel). Figure 4.3 (top panels) shows 12 consecutive near-nadir (view-zenith angle < 20°) overpasses of Riyadh. OMI measures high NO_2 directly over Riyadh, and in general, the observed plume flows and decays along the direction of the observed winds. As an aside, we note that daily OMI NO_2 measurements appear to be of a quality that they could be used as constraints on the assimilated wind fields. Certainly the higher resolution images expected from future geostationary satellites will be useful in that regard (e.g., Valin et al., 2011a).

The spatial pattern and gradients of the average NO_2 column (Fig. 4.3 – bottom panel) reflect transport patterns and the nonlinear effects of chemistry. To control for variations of wind direction, Beirle et al. (2011) computed spatially distinct NO_2 column averages by grouping OMI measurements according to the surface wind direction (e.g., N, NE, E, etc.), computing an average NO_x lifetime for each wind direction. Here, we extend that idea and control for both wind speed and wind direction. Instead of defining and averaging along 8 separate vectors, we rotate each OMI measurement so that the mean wind is aligned in the x-direction and centered over Riyadh (Fig. 4.4). We then sort the observations in to six separate wind speed categories (0 – 7 km hr^{-1}, 7 – 11 km hr^{-1}, 11 – 14 km hr^{-1}, 14 – 18 km hr^{-1}, 18 – 23 km hr^{-1}, 23 – 30 km hr^{-1}). There are between 35 and 50 high-quality cloud-free observations for each of the six selected ranges of wind speed for April through September 2005 – 2011.

Figure 4.4 shows the aligned NO_2 column when winds are slow (7 – 11 km hr^{-1}) and when winds are fast (23 – 30 km hr^{-1}) as well as the integrated NO_2 column density perpendicular to the mean flow (i.e., the NO_2 line density) and the total NO_2 mass for all six wind speed categories. OMI observes significant variation of the NO_2 column with wind speed demonstrating the capacity of space-based observations to capture atmospheric evolution over a source. In slow winds (7 – 11 km hr^{-1}), the NO_2 columns observed directly over Riyadh are more than double those observed in fast winds (23 – 30 km hr^{-1}), an indication of both atmospheric stagnation and differences in NO_x removal. When wind speeds are fastest, the influence of sources in Riyadh extends much further downwind, with columns exceeding 1.5×10^{15} molecules cm^{-2} extending more than 250 km downwind. The effect of wind speed on the pattern of the observed NO_2 columns is ordered and clear, with the columns decreasing and extending further from the source as wind speeds increase. This is an important demonstration of the quality of the OMI measurements and of the re-analysis winds.

To determine the effective plume-average NO_x lifetime, we analyze the spatial evolution of the NO_2 line density downwind of Riyadh (Fig. 4.4 – third panel). When winds are slow, the rise and fall of the NO_2 line density is nearly Gaussian, a reflection of variable winds in addition to the chemical removal of NO_x making an accurate estimate of the NO_x lifetime difficult. Instead we analyze the pattern when winds are fast. When winds are fast (lightest-gray; 23 – 30 km hr^{-1}) the downwind decay is dominated by chemical removal, not variability in wind direction. NO_2 decays from its maximum by one e-fold over a distance of 145 km. This rate of decay corresponds to a NO_x lifetime of 5.5 hours. By distinguishing measurements based on surface

wind speed, we avoid introducing artificial gradients that would result from averaging the patterns observed in slow, stagnant conditions (e.g. Fig. 4.4 – top panel) with those observed in fast wind conditions (e.g. Fig. 4.4 – second panel).

To examine the NO_x lifetime at slower wind speeds, we assume that the rate of NO_x emissions does not vary with wind speed and investigate the variation of the observed mass (Fig. 4.4 – bottom panel). We scale the results to our inference from the experimental decay observed in rapid winds and find the lifetime increases from 5.5 hours in fast winds to 8.0 hours in slow winds. This finding is consistent with the idea that the speed of wind determines the dilution rate of NO_x which affects the OH concentration (Fig. 4.1). The magnitude and the direction of the observed lifetime increase (30%) is in good agreement with the magnitude of variations predicted in a model when urban sources are artificially diluted via model grid spacing (Valin et al., 2011b). We find the NO_x lifetime averaged over all wind conditions is 6.7 hours. If we assume that NO_2 is only removed by OH ($k_{NO2+OH} = 9.2\times10^{-12}$ cm^3 $molecule^{-1}$ s^{-1}) and that the steady-state ratio of NO_2 to NO_x is 0.72, this lifetime corresponds to an effective OH concentration of 6.25×10^6 molecules cm^{-3}.

We compute the NO_x emission rate by mass balance and by mass flux restricting our analysis to the fastest wind conditions. For both methods, we assume a fixed ratio of NO_2 to NO_x (0.72). By mass balance, the amount of NO_2 observed over Riyadh in fast winds (Fig. 4.4 – bottom panel) corresponds to a NO_x emission rate of 135 moles s^{-1} given the NO_x lifetime of 5.5 hours. By mass flux, the maximum NO_2 enhancement (1.24×10^4 moles km^{-1}; Fig. 4.4 – third panel) observed 25 km downwind of Riyadh corresponds to a NO_x flux of 126 moles s^{-1} given winds of 26 km hr^{-1}. Agreement between these two values indicates that very little NO_x is removed during the 1 hr transit from the Riyadh center to the location 25 km downwind.

4.4 Discussion

Simultaneously inferring the rate of NO_x emissions and removal directly from satellite-based measurements of the NO_2 column has been discussed previously (e.g., Leue et al., 2001; Beirle et al., 2004; Beirle et al., 2011). In the approach described here, we restrict our analysis of spatial patterns used to simultaneously infer NO_x emissions and lifetime to measurements made when winds are fast. We then infer the NO_x lifetime in slower wind conditions by mass balance. Beirle et al. (2011) analyzed the average spatial pattern of measurements made in all wind speeds.

We show that steep nonlinearities in the NO_x lifetime as controlled by NO_2 concentrations are evident in the measurements (Fig. 4.4 – bottom panel). Our observation that the lifetime of NO_x depends on wind speed (a surrogate for the rate of atmospheric mixing) confirms that the concentration of NO_x-sinks such as OH, RO_2 and $RC(O)O_2$ depend on the concentration of NO_x (Fig. 4.1). The finding that there are different lifetimes for different wind speeds and that the average lifetime and average NO_2 do not exist is a well known mathematical consequence of covariance among variables, i.e. the product of the average is not equal to the average of the products. In this case, meteorological and chemical variability directly affect the relationship of OH and NO_x, such that inference of OH concentration from the average NO_2 spatial pattern is not the same as what would be inferred from individual measurements. As a consequence, we infer a longer average NO_x lifetime (6.7 hours vs. 4 hours) over Riyadh and a correspondingly lower emission rate (135 moles s^{-1} vs. 260 moles s^{-1}) than did Beirle et al. [2011]. Most of the difference between the inferred emission rates (~75%) follows from our treatment of the lifetime

as wind-speed dependent. A smaller fraction (~25%) results from systematic biases between DOMINO v1.02 and DOMINO V2.0 (Boersma et al., 2011).

4.5 Conclusions

Using the example of Riyadh, Saudi Arabia, we show that it is possible to simultaneously infer the NO_x lifetime and emissions from space-based observations. We find that the lifetime is wind-speed dependent. The spatial extent of the Riyadh plume is much larger than 13×24 km^2 OMI footprint or the 30×50 km^2 extent of Riyadh, such that neither instrument spatial resolution nor urban extent is limiting the interpretation of NO_x loss processes from the spatial patterns of NO_2 column. A variety of other meteorological factors affect the NO_x lifetime including water vapor, O_3, sunlight, boundary layer height and temperature. We expect future analyses will be able to untangle the effects of these variables on the NO_x lifetime.

References

Beirle, S., Platt, U., von Glasow, R., Wenig, M., and Wagner, T.: Estimate of nitrogen oxide emissions from shipping by satellite remote sensing, Geophysical Research Letters, 31, L18102, 2004.

Beirle, S., Huntrieser, H., and Wagner, T.: Direct satellite observation of lightning-produced NOx, Atmospheric Chemistry and Physics, 10, 10965-10986, 2010.

Beirle, S., Boersma, K. F., Platt, U., Lawrence, M. G., and Wagner, T.: Megacity Emissions and Lifetimes of Nitrogen Oxides Probed from Space, Science, 333, 1737-1739, 2011.

Bertram, T. H., Heckel, A., Richter, A., Burrows, J. P., and Cohen, R. C.: Satellite measurements of daily variations in soil NOx emissions, Geophysical Research Letters, 32, L24812, 2005.

Boersma, K., Eskes, H., Dirksen, R., van der A, R., Veefkind, J., Stammes, P., Huijnen, V., Kleipool, Q., Sneep, M., Claas, J., Leitao, J., Richter, A., Zhou, Y., and Brunner, D.: An improved tropospheric NO_2 column retrieval algorithm for the Ozone Monitoring Instrument, Atmospheric Measurement Techniques, 4, 1905-1928, 2011.

Boersma, K. F., Eskes, H. J., Veefkind, J. P., Brinksma, E. J., van der A, R. J., Sneep, M., van den Oord, G. H. J., Levelt, P. F., Stammes, P., Gleason, J. F., and Bucsela, E. J.: Near-real time retrieval of tropospheric NO_2 from OMI, Atmospheric Chemistry and Physics, 7, 2103-2118, 2007.

Bucsela, E. J., Pickering, K. E., Huntemann, T. L., Cohen, R. C., Perring, A., Gleason, J. F., Blakeslee, R. J., Albrecht, R. I., Holzworth, R., Cipriani, J. P., Vargas-Navarro, D., Mora-Segura, I., Pacheco-Hernandez, A., and Laporte-Molina, S.: Lightning-generated NOx seen by the Ozone Monitoring Instrument during NASA's Tropical Composition, Cloud and Climate Coupling Experiment (TC4), Journal of Geophysical Research-Atmospheres, 115, 2010.

Castellanos, P., and Boersma, K. F.: Reductions in nitrogen oxides over Europe driven by environmental policy and economic recession, Scientific Reports, 2, 7, 2012.

Choi, Y., Wang, Y. H., Zeng, T., Martin, R. V., Kurosu, T. P., and Chance, K.: Evidence of lightning NOx and convective transport of pollutants in satellite observations over North America, Geophysical Research Letters, 32, L02805, 2005.

Dee, D., Uppala, S., Simmons, A., Berrisford, P., Poli, P., Kobayashi, S., Andrae, U., Balmaseda, M., Balsamo, G., Bauer, P., Bechtold, P., Beljaars, A., van de Berg, L., Bidlot, J., Bormann, N., Delsol, C., Dragani, R., Fuentes, M., Geer, A., Haimberger, L., Healy, S., Hersbach, H., Holm, E., Isaksen, L., Kallberg, P., Kohler, M., Matricardi, M., McNally, A., Monge-Sanz, B., Morcrette, J., Park, B., Peubey, C., de Rosnay, P., Tavolato, C., Thepaut, J., and Vitart, F.: The ERA-Interim reanalysis: configuration and performance of the data assimilation system, Quarterly Journal of the Royal Meteorological Society, 137, 553-597, 2011.

Hudman, R. C., Russell, A. R., Valin, L. C., and Cohen, R. C.: Interannual variability in soil nitric oxide emissions over the United States as viewed from space, Atmos. Chem. Phys., 10, 9943-9952, 2010.

Hudman, R. C., Moore, N. E., Mebust, A. K., Martin, R. V., Russell, A. R., Valin, L. C., and Cohen, R. C.: Steps towards a mechanistic model of global soil nitric oxide emissions:

implementation and space based-constraints, Atmospheric Chemistry and Physics, 12, 7779-7795, 2012.

Jaegle, L., Steinberger, L., Martin, R. V., and Chance, K.: Global partitioning of NO_x sources using satellite observations: Relative roles of fossil fuel combustion, biomass burning and soil emissions, Faraday Discussions, 130, 407-423, 2005.

Kim, S. W., Heckel, A., Frost, G. J., Richter, A., Gleason, J., Burrows, J. P., McKeen, S., Hsie, E. Y., Granier, C., and Trainer, M.: NO_2 columns in the western United States observed from space and simulated by a regional chemistry model and their implications for NO_x emissions, Journal of Geophysical Research-Atmospheres, 114, 29, D11301, 2009.

Lamsal, L. N., Martin, R. V., Padmanabhan, A., van Donkelaar, A., Zhang, Q., Sioris, C. E., Chance, K., Kurosu, T. P., and Newchurch, M. J.: Application of satellite observations for timely updates to global anthropogenic NO_x emission inventories, Geophysical Research Letters, 38, 2011.

Leue, C., Wenig, M., Wagner, T., Klimm, O., Platt, U., and Jahne, B.: Quantitative analysis of NO_x emissions from Global Ozone Monitoring Experiment satellite image sequences, Journal of Geophysical Research-Atmospheres, 106, 5493-5505, 2001.

Martin, R. V., Jacob, D. J., Chance, K., Kurosu, T. P., Palmer, P. I., and Evans, M. J.: Global inventory of nitrogen oxide emissions constrained by space-based observations of NO_2 columns, Journal of Geophysical Research-Atmospheres, 108, 4537, 2003.

Mebust, A. K., Russell, A. R., Hudman, R. C., Valin, L. C., and Cohen, R. C.: Characterization of wildfire NOx emissions using MODIS fire radiative power and OMI tropospheric NO2 columns, Atmospheric Chemistry and Physics, 11, 5839-5851, 2011.

Miyazaki, K., Eskes, H. J., and Sudo, K.: Global NO_x emission estimates derived from an assimilation of OMI tropospheric NO_2 columns, Atmospheric Chemistry and Physics, 12, 2263-2288, 2012.

Murphy, J. G., Day, D. A., Cleary, P. A., Wooldridge, P. J., Millet, D. B., Goldstein, A. H., and Cohen, R. C.: The weekend effect within and downwind of Sacramento: Part 2. Observational evidence for chemical and dynamical contributions, Atmos. Chem. Phys. Discuss., 6, 11971-12019, 2006.

Perring, A. E., Bertram, T. H., Farmer, D. K., Wooldridge, P. J., Dibb, J., Blake, N. J., Blake, D. R., Singh, H. B., Fuelberg, H., Diskin, G., Sachse, G., and Cohen, R. C.: The production and persistence of Sigma RONO2 in the Mexico City plume, Atmospheric Chemistry and Physics, 10, 7215-7229, 2010.

Russell, A., Valin, L., and Cohen, R.: Trends in OMI NO_2 observations over the US: effects of emission control technology and the economic recession, Atmospheric Chemistry and Physics Discussions, 12, 15419-15452, 2012.

Stavrakou, T., Muller, J. F., Boersma, K. F., De Smedt, I., and van der A, R. J.: Assessing the distribution and growth rates of NO_x emission sources by inverting a 10-year record of NO_2 satellite columns, Geophysical Research Letters, 35, 2008.

Valin, L., Russell, A., Bucsela, E., Veefkind, J., and Cohen, R.: Observation of slant column NO2 using the super-zoom mode of AURA-OMI, Atmospheric Measurement Techniques, 4, 1929-1935, 2011a.

Valin, L., Russell, A., Hudman, R., and Cohen, R.: Effects of model resolution on the interpretation of satellite NO_2 observations, Atmospheric Chemistry and Physics, 11, 11647-11655, 2011b.

van der A, R. J., Eskes, H. J., Boersma, K. F., van Noije, T. P. C., Van Roozendael, M., De Smedt, I., Peters, D., and Meijer, E. W.: Trends, seasonal variability and dominant NO_x source derived from a ten year record of NO_2 measured from space, Journal of Geophysical Research-Atmospheres, 113, D04302, 2008.

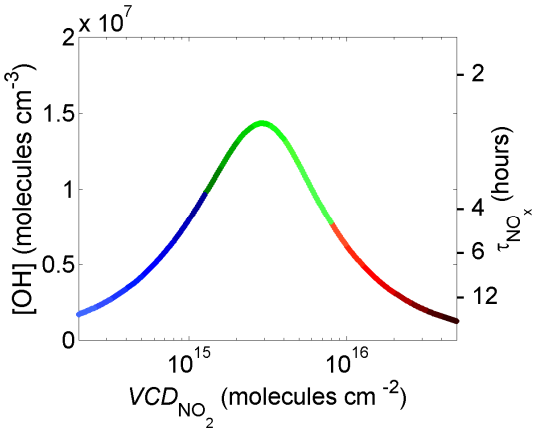

Figure 4.1 The steady-state relationship of OH concentration (right axis) and the NO_x lifetime (left axis) to the NO_2 column density, assuming a 1 km, well-mixed boundary layer, under conditions typical of a polluted summertime urban environment (Murphy et al., 2006; Valin et al., 2011b). The lifetime is computed with respect to reaction of NO_2 with OH and an NO_2 to NO_x ratio of 0.72. The color scale used here is used for images of NO_2 column throughout the article.

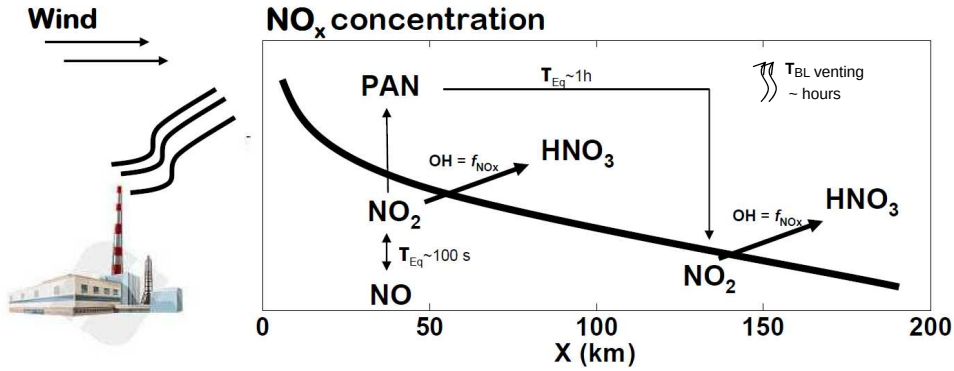

Figure 4.2 A depiction of NO_x chemistry downwind of an emission source.

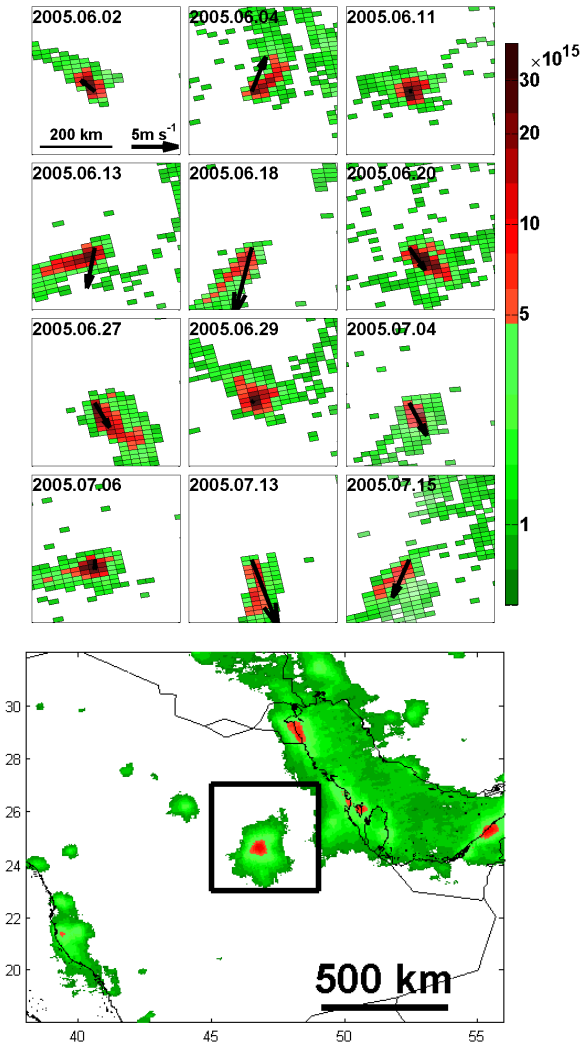

Figure 4.3 (Top 12 panels) NO_2 column for the first 12 near-nadir overpasses over Riyadh (45°–49° E, 23°–27° E) beginning June 2, 2005 and (bottom panel) the Summer 2005 average including the surrounding region. Measurements below 1.5×10^{15} molecules cm^{-2} are not shown. For the daily measurements, OMI-observed cloud fractions are indicated with transparency: cloud fractions greater than 20% are fully transparent and equal to 0% are fully opaque. For daily measurements, the interpolated 12 PM LST winds from the 1.5° × 1.5° surrounding Riyadh are plotted (scale in the top-left panel).

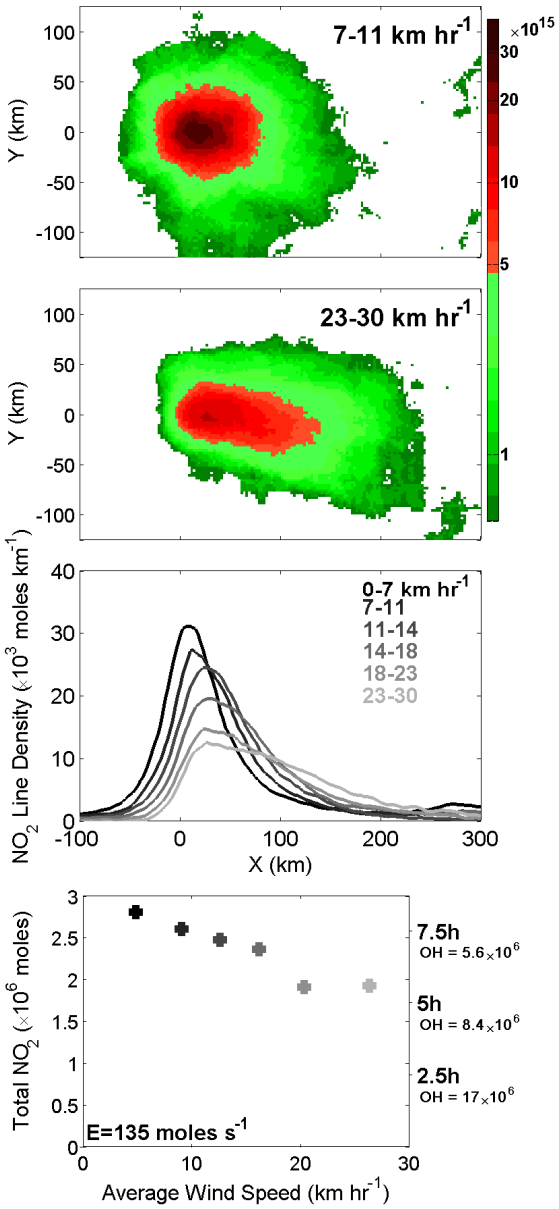

Figure 4.4 April-September 2005-2011 wind-aligned NO_2 column density when winds are slow (top-panel, 7 –11 km hr^{-1}) and fast (second panel, 23 – 30 km hr^{-1}), (third panel) the NO_2 column density integrated perpendicular to the mean flow, i.e., the NO_2 line density, for all six wind speed categories, and (bottom panel) the total NO_2 enhancement for each range of wind speeds (left axis) with the corresponding NO_x lifetime and effective OH concentration indicated (right axis) given an emission rate of 135 moles s^{-1}. An experimentally determined background of 0.93×10^{15} molecules cm^{-2} is subtracted from all measurements.

Chapter 5 – Chemical feedback effects on the spatial patterns of the NO_x weekend effect

5.1 Introduction

In the troposphere, NO_x ($NO+NO_2$) affects ozone production rates, aerosol formation and the oxidative capacity of the atmosphere. NO_x is emitted to the troposphere by fossil-fuel combustion, biomass burning, soil microbial processes, and lightning. During the daytime NO_x is removed from the atmosphere by reactions of HO_x ($OH+HO_2+RO_2$) with NO_x, primarily by reaction of OH with NO_2 to form nitric acid, $RC(O)O_2$ with NO_2 to form acylperoxy nitrates, and RO_2 with NO to form alkyl nitrates. As a result, the chemical removal of NO_x depends on the concentration of OH and the local mix of volatile organic compound (VOC) precursors to $RC(O)O_2$ and RO_2 (e.g., Browne and Cohen, 2012). Both OH and RO_2 depend non-linearly on NO_x introducing a powerful nonlinear feedback of NO_x on its own lifetime (Fig. 5.1).

Satellite-based observation of the NO_2 column has provided a wealth of information on NO_x at local (e.g., Bertram et al., 2005; Boersma et al., 2009; Russell et al., 2012), regional (e.g., Richter et al., 2005; Kim et al., 2009; Hudman et al., 2010), and global scales (e.g., Stavrakou et al., 2008; Lamsal et al., 2011). Satellite-based instruments have proved particularly useful in measuring seasonal (e.g., Jaegle et al., 2005; van der A et al., 2006), interannual (e.g., Richter et al., 2005; van der A et al., 2008; Russell et al., 2012), and day-of-week (e.g., Beirle et al., 2003; Kaynak et al., 2009; Russell et al., 2010) trends in NO_2 column. Typically, the observed columns and their trends are used to assess differences in NO_x emissions, but much less attention has been paid to a secondary driver of the trend, changes in the NO_x lifetime. In situ observations (e.g., Thornton et al., 2002; Murphy et al., 2007) have provided extensive information on the mechanistic details of these effects on the NO_x lifetime, but lack coverage in space and time. With a nadir footprint of 13×24 km^2 and daily, global coverage, the Ozone Monitoring Instrument (OMI; Levelt et al., 2006) is uniquely capable of providing coverage and spatial detail at a scale relevant to boundary layer NO_x removal (~10 km–50 km; e.g., Ryerson et al., 2001; Dillon et al., 2002; Beirle et al., 2011; Valin et al., 2011a; Valin et al., 2011b) .

Here, we use OMI observations to describe the spatial variation of the NO_2 column over Los Angeles on weekends and weekdays. We then use a series of WRF-Chem model simulations to characterize the information contained in the day-of-week patterns. From the range of simulations computed, we identify modifications to the base model that produce improved matches to the OMI observations and use this to guide our understanding of the chemical processes that control the NO_2 column.

5.2 Observations

The Ozone Monitoring Instrument (OMI), a UV/VIS spectrometer developed at KNMI in the Netherlands (Levelt et al., 2006), is mounted on the polar-orbiting, sun-synchronous NASA Aura satellite (Schoeberl et al., 2006). OMI has a 114° field-of-view, with 480 detector elements devoted to spatial coverage that are averaged onboard to provide 60 pixels across a 2600 km swath of the earth , and a 2 second integration period that results in a 13 km pixel dimension in the direction of the spacecraft motion. The resulting spatial footprint is as small as 13×24 km^2. Aura/OMI orbits the earth over 14 times a day providing near global coverage at approximately 1:15 PM local solar time.

Several different analyses of the spectrum measured by OMI are publically available (Bucsela et al., 2006; Boersma et al., 2007; Russell et al., 2011). Here, we use the BErkeley High

Resolution (BEHR) retrieval of OMI NO_2 vertical tropospheric columns (available at http://behr.cchem.berkeley.edu) (Russell et al., 2011; Russell et al., 2012). Briefly, BEHR derives tropospheric vertical NO_2 column from the NASA standard tropospheric slant column (Bucsela et al., 2006) using high spatial resolution inputs to the Standard Product AMF lookup table, specifically 12×12 km^2 monthly-averaged vertical NO_2 profiles, 0:05°×0:05° 16-day average MODIS albedo product (MCD43C3), and the Global Land One-kilometer Base Elevation (GLOBE) Digital Elevation Model. Here, we use BEHR version 1.0B. The version number corresponds with the Standard Product version used to derive BEHR, and the version letter corresponds to the version of BEHR for a given Standard Product version.

Figure 5.2 shows the average May-July, 2005-2007 weekday NO_2 column (Monday – Friday), the weekend column (Saturday – Sunday), and the pattern of weekend NO_2 column decreases observed by OMI over Southern California. We include a true-color Aqua-MODIS image of the region observed on a cloud-free day (29 May 2005). The Greater Los Angeles metropolitan area consists of three distinct basins: the Los Angeles Basin at the coast (33.8°–34.1° N, 117.8°–118.4° W), the San Fernando Valley to the northwest (34.1°–34.3° N, 118.2°–118.8° W), and the San Bernardino Valley to the East (33.8°–34.2° N, 117.0°–117.8° W). During the summer, the typical daytime meteorology consists of onshore flow entering the Los Angeles basin at the coast flowing out through the San Bernardino Valley to the east and the San Fernando Valley to the northwest.

Due to the onshore flow and large coastal emission sources, the weekday NO_2 column increases sharply at the coastline to a maximum of 3.9×10^{16} molecules cm^{-2} directly over downtown Los Angeles (Fig. 5.2b). In the San Bernardino Valley, NO_2 columns decrease gradually. Decreases in the San Fernando Valley are sharper than in San Bernardino. Over a long-term average the airflow on weekends is identical to that on weekdays. The weekend NO_2 column is markedly lower than the weekday column and the gradients downwind of central Los Angeles are much steeper. Weekend decreases of the NO_2 column are only 30-40% over coastal Los Angeles but are 45-55% over the San Fernando Valley and an even larger 55-65% over the San Bernardino Valley.

Large decreases of the NO_2 column and surface concentration have been reported previously using satellite and in situ observations (e.g., Beirle et al., 2003; Murphy et al., 2007; Russell et al., 2010). The changes have been attributed primarily to a day-of-week pattern of emissions, with decreases in the U.S. associated with a reduction in freight transport by heavy-duty diesel powered. These decreases of NO_x affect the chemical feedbacks on OH and O_3 (e.g., Stephens et al., 2008; Valin et al., 2011b; Pollack et al., 2012; Pusede and Cohen, 2012, and references therein). However, the observation that the NO_2 decreases are not spatially uniform, an observation that OMI is uniquely capable of capturing with its spatial detail, has not, to our knowledge, been previously reported or evaluated. In the following, we simulate the day-of-week pattern of NO_2 column using WRF-Chem and compare the results to the observations in an effort to understand which model parameters are important for describing the day-of-week patterns in Los Angeles, and by analogy, for describing day-of-week patterns of NO_2 in other locations.

5.3 WRF-Chem Calculations

We simulate the NO_2 column at the OMI overpass time (1 PM) using WRF-Chem (Grell et al., 2005) at 4 km horizontal resolution over a 288 km (N-S) by 480 km (E-W) domain, centered

at 34° N, 118° W. We use 36 vertical layers, 14 of which are in the first 1.5 km. As our base case, we use the Regional Acid Deposition Model 2 (RADM2) chemical mechanism, the 2005 National Emissions Inventory (NEI2005) for anthropogenic emissions and the default online module for biogenic emissions as in Grell et al. (Grell et al., 2005). Initial and boundary conditions for meteorology are taken from the North American Regional Reanalysis (NARR) and for chemistry are taken from an idealized profile standard to WRF-Chem.

We simulate the average 1 PM NO_2 column for 1-14 June 2008 with NEI2005 anthropogenic emissions (weekday) and the same model with an emission rate of $0.625 \times E_{NOx\text{-}NEI2005}$ (weekend). The first two days are used as spin-up. For the base case, we run WRF-Chem with standard RADM2 chemistry and spatially and temporally uniform weekend emission reductions. We compare results from this base case calculation to weekday/weekend simulations in which we adjust HO_x production from ozone photolysis (0.5×, 1.25×, 1.5×, 2×), VOC emissions (0.5×, 2×), VOC–OH rate constants (0.5×, 2×), the NO_2–OH rate constant (0.5×, 2×), the timing of weekend emissions (1 h delay, 2 h delay), and the spatial distribution of weekend emissions (Weekend $E_{NOx–San\ Bernardino}$ 0.575×, 0.525× $E_{NOx\text{-}NEI2005}$, and $E_{NOx–Los\ Angeles}$ 0.640×,0.654× $E_{NOx\text{-}NEI2005}$, for domain-average weekend emission of 0.625× $E_{NOx\text{-}NEI2005}$). The results from these simulations and the OMI observations are summarized in Table 5.1. Table 5.1 reports the total reduction of NO_2 column over the entire Los Angeles plume (defined as the area over which OMI-observes weekday NO_2 columns exceeding 2.5×10^{15} molecules cm^{-2}) and the fraction of the Los Angeles plume with weekend decreases of NO_2 column that exceed 35%, 45%, and 55%.

We find that the simulated NO_2 columns, regardless of model scenario, are biased low where NO_2 is low. To correct this bias we add a regionally uniform background column of 5×10^{14} molecules cm^{-2} to the both weekday and weekend simulations for all model scenarios. This correction does not significantly impact model results where the NO_2 columns are high, but does alter the simulated spatial patterns at the edges of the plume where NO_2 is low (~20 % effect where NO_2 columns are 2.5×10^{15} molecules cm^{-2}). We test whether a two week period of simulation is representative of longer time periods by simulating the base case scenario for three months and find that the magnitude and pattern of decreases simulated in the two-week scenario is comparable to that of the 3-month scenario indicating its fidelity in representing the meteorological variability of a longer-term simulation. We also test for memory effects. We simulate weekday NO_2 column in two-day periods (June 3-4, June 4-5, …, June 13-14) initialized with the model NO_2 column from 4PM LST on the previous weekday to test whether simulation of 14 consecutive weekend days is biased relative to simulation of two-day weekends within a weekly cycle. We find that the memory effect of weekday emissions on weekend column is small compared to the effects of the other parameters tested.

5.4 Model Results and Analysis

In Figure 5.3, we compare the observed day-of-week pattern of NO_2 column (top row) to that simulated with the base model (second row). Integrated over the entire basin, there is only a 2% difference between observation and simulation and both exhibit similar spatial patterns. Locally, however, there are large differences between the simulated and observed NO_2 columns (up to a factor of two). OMI observes much higher NO_2 values on the south and west edges of the plume, and the model predicts much higher values in the outflow regions, namely the southeast and northwest edges of the plume. This discrepancy indicates several possible model or observational uncertainties. For instance, NO_2 may be transported downwind too quickly in the

model, the observations may be biased over the coastline (e.g., solar glint reflectance impacts on the NO_2 retrieval), or OMI with its pixels of 13×24 km^2 may be smearing the spatial pattern that is simulated at a model horizontal resolution of 4×4 km^2 even though our average of the OMI data takes advantage of oversampling to increase the resolution to approximately 10×10 km^2.

The large, localized differences between the observed and simulated NO_2 columns highlight the difficulty of accurately computing the interplay of emissions, chemistry and transport or of accounting for the possibility of locally-specific observational biases. However, when investigating the patterns of NO_2 column (e.g., day-of-week effect) with self-consistent model simulations or observational datasets, many of these biases are eliminated. In our WRF-Chem model setup, for instance, the weekday and weekend meteorology is identical, and over a long time period, OMI observes weekday and weekend NO_2 columns that are subject to the same average meteorological patterns and the same average observational biases. As a result, the agreement of modeled and simulated NO_2 trends (e.g., day-of-week effect; Fig. 5.3 – right column) is more meaningful than the agreement of observations and simulation over a single time period (e.g., weekday NO_2 column; Fig. 5.3 – left column). In the base model, simulated NO_2 decreases are too large over the coast (40% vs. <35%), are too small over San Bernardino (50% vs. 60%), and extend too far inland (150 km vs. 100 km).

The day-of-week pattern of the NO_2 column depends both on patterns of NO_x removal and patterns of NO_x emissions. The pattern of removal depends on the relationship of OH and RO_2 concentrations to NO_x (Fig. 5.1). In Los Angeles, where NO_x concentrations are high (i.e., to the right side of the NO_x-OH curve), a decrease of NO_x emissions on the weekends results in higher concentrations of OH and RO_2. As a result, NO_x is removed faster, and the reduction of NO_2 columns on the weekend is larger than the reduction of NO_x emissions alone. The spatial map of these nonlinear effects reflects the timescale for NO_x removal (Fig. 5.3 – right column). If the chemical removal of NO_x is slow, the nonlinear decreases will be small over the source where NO_x concentrations are high, but will persist and accumulate far downwind where the concentrations eventually decrease to a value that corresponds to a maximum OH concentration and a minimum in the NO_x chemical lifetime (Fig. 5.1). If the chemical removal of NO_x is rapid near the source, the nonlinear feedbacks will be large in that location. The discrepancy between the observations and the base simulation (Fig. 5.3 – first row vs. second row) suggests that the model falls into the first category while the observations fall into the second category, an indication that the simulated OH and RO_2 concentrations are too low (i.e., the model is too far to the right of the NO_2-OH curve presented in Figure 5.1).

To test this hypothesis, we evaluate the effects of parameters that influence the concentration of OH and RO_2, and thus affect the timescale of NO_x removal. We double the rate of ozone photolysis to increase the concentration of OH and RO_2 (i.e. shift the entire NO_2-OH curve in Figure 5.1 upward). Separately, we double the anthropogenic emissions of VOC to increase the concentration of RO_2 throughout the model domain.

Figure 5.3 (third row) shows the simulated day-of-week pattern of the NO_2 column when HO_x production is increased. Due to the increase of HO_x, the rate of NO_x removal increases, and both weekday and weekend NO_2 columns are smaller than those simulated in the base model. As a result of higher OH and RO_2, the timescale of NO_x losses is shortened compared to the timescale of transport, and, as hypothesized, the weekend decrease is larger near the source and does not extend as far downwind relative to the base case. Here, we adjust HO_x production using ozone

photolysis, but other sources of HO_x (or Cl), such as HONO, $ClNO_2$, or HCHO photolysis may play a role.

Figure 5.3 (fourth row) shows the simulated day-of-week pattern of the NO_2 column when VOC emissions are doubled. VOC both removes OH and leads to OH formation through its feedback on HO_x sources (e.g., O_3, formaldehyde). At low NO_x concentrations, the role of VOC as a sink of OH dominates, and OH decreases for any increase of VOC. At high NO_x, however, the role of VOC as a sink of OH is small, and the concentration of OH increases with increases of VOC. As a result, RO_2 increases everywhere for an increase of VOC emissions, and OH increases where NO_x is high (NO_2 column > 7.5×10^{15} molecule cm^{-2}) but decreases where NO_x is low (NO_2 column < 5×10^{15} molecule cm^{-2}). Due to higher OH and RO_2 concentrations over Los Angeles, the timescale of NO_2 removal is shortened when VOC emissions are increased relative to the base model, and the agreement of the simulated day-of-week pattern with observations improves. Here, we alter VOC concentrations by altering anthropogenic VOC emissions, but biogenic emissions may also be a significant source of VOC in Los Angeles.

The comparison of modeled and observed day-of-week patterns of the NO_2 column suggest that HO_x chemistry in Los Angeles is NO_x-saturated (Fig. 5.1), but also indicate that the Los Angeles atmosphere is not as far to the right of the NO_x-OH-RO_2 relationship as the model simulation. We find that agreement between model and observation is improved when we increase HO_x production or VOC emissions in the model, but the improvement is similar for both changes (Fig. 5.3 – third row vs. fourth row). Despite their similarities, there are significant differences between these two adjustments, particularly differences in the relative roles of RO_2 and OH as NO_x sinks (i.e., PAN and $RONO_2$ vs. HNO_3). PAN, for example, is thermally unstable and is much more likely to re-release NO_x downwind than is HNO_3, which is more likely to deposit before undergoing photolysis or reaction with OH. Distinguishing the roles of HNO_3 and PAN chemistry may require more information, such as higher spatial resolution satellite-based measurements at the plume edges where the differences between the two simulations seem the largest or time resolved measurements as will become available from geostationary orbit (e.g., GEO-CAPE; Fishman et al., 2008).

The day-of-week pattern of NO_2 columns also depends on day-of-week patterns of emissions. The timing of emissions shifts later in the day on weekends (Harley et al., 2005). The delay of emissions on weekends relative to weekdays is expected from a shift of light-duty gasoline vehicle activity later in the day. Weekend emission reductions also vary regionally, and likely locally, due to differing day-of-week trends in industry and heavy-duty diesel truck activity relative to passenger vehicle activity (McDonald et al., 2012).

Figure 5.3 (fifth row) shows the day-of-week pattern of NO_2 simulated when we delay the timing of all weekend emissions, both VOC and NO_x, by two hours. When weekend emissions are delayed, the 1 PM NO_2 column decreases because the total emissions in the hours prior to the satellite overpass decrease. The timing of emissions affects the magnitude of the observed decreases but does not significantly affect the spatial pattern.

Figure 5.3 (sixth row) shows the day-of-week pattern of NO_2 calculated with a different weekend emission reduction aver San Bernardino ($0.525 \times E_{NOx\text{-}NEI2005}$) than over Los Angeles ($0.654 \times E_{NOx\text{-}NEI2005}$) where the total weekend emission reduction is no different than the base case ($0.625 \times E_{NOx\text{-}NEI2005}$). Not surprisingly, the contrast between the East basin (San Bernardino) and the West basin (Los Angeles) is larger when the regional day-of-week emission

pattern is altered, a modest effect, but one that is consistent with observations that show larger decreases over San Bernardino and smaller decreases over the Los Angeles basin. This pattern might be used in conjunction with detailed vehicle activity assessments to understand whether the changes are consistent with a differential weekend decrease of heavy-duty diesel truck traffic in the two regions.

In the set of simulations discussed above, we show that the NO_2 column and more specifically day-of-week patterns of NO_2 column depend strongly on HO_x production, VOC, and the timing and spatial distribution of weekend emissions. While no single modification provides an unbiased representation of the observed day-of-week pattern over Los Angeles, our comparison of the simulated and observed patterns provides a framework for future work aimed at optimally reproducing the day-of-week pattern of NO_2 column over Los Angeles or any location.

5.5 Conclusions

The high spatial resolution of OMI (13×24 km^2) captures a phenomenal level of detail over the Los Angeles metropolitan area (200×150 km^2). Comparisons of these observations to a high resolution model demonstrate that this spatial detail provides information on local patterns of NO_x transport, emissions and chemistry. The observations show that weekend decreases of NO_2 column are smallest over central Los Angeles (30-40%) where NO_2 columns are high, and are largest downwind of Los Angeles over the San Bernardino and San Fernando Valleys (50-65%).

Using WRF-Chem, we simulate weekday and weekend NO_2 column using a range of model parameters. In the model, the weekend NO_2 column decreases by more than the weekend emissions reduction, a nonlinear feedback that results from the increase of OH concentration and the corresponding decrease of NO_x lifetime that occur when NO_x concentrations are reduced. We show that simulated pattern of weekend NO_2 decreases is sensitive to HO_x production, VOC emissions, and the spatiotemporal distribution of NO_x emissions. The magnitude of the simulated day-of-week pattern of column NO_2 is in better agreement with observations when HO_x production is increased, when VOC emissions are increased, or when weekend emissions are delayed or shifted spatially. This is a unique conclusion indicating that satellite measurements of NO_2 can simultaneously teach us about day-of-week trends in NO_x emissions and the coupled day-of-week variation of the NO_x lifetime.

Further work should focus on the evolution of day-of-weekend NO_2 patterns over time. Its seasonal evolution, for instance, can teach us about chemical feedbacks, as seasonal variations of day-of-week emission trends are expected to be small. The interannual evolution, on the other hand, would provide an additional set of constraints on emission trends and the NO_x lifetime.

References

Beirle, S., Platt, U., Wenig, M., and Wagner, T.: Weekly cycle of NO2 by GOME measurements: a signature of anthropogenic sources, Atmospheric Chemistry and Physics, 3, 2225-2232, 2003.

Beirle, S., Boersma, K. F., Platt, U., Lawrence, M. G., and Wagner, T.: Megacity Emissions and Lifetimes of Nitrogen Oxides Probed from Space, Science, 333, 1737-1739, 2011.

Bertram, T. H., Heckel, A., Richter, A., Burrows, J. P., and Cohen, R. C.: Satellite measurements of daily variations in soil NOx emissions, Geophysical Research Letters, 32, L24812, 2005.

Boersma, K. F., Eskes, H. J., Veefkind, J. P., Brinksma, E. J., van der A, R. J., Sneep, M., van den Oord, G. H. J., Levelt, P. F., Stammes, P., Gleason, J. F., and Bucsela, E. J.: Near-real time retrieval of tropospheric NO2 from OMI, Atmospheric Chemistry and Physics, 7, 2103-2118, 2007.

Boersma, K. F., Jacob, D. J., Trainic, M., Rudich, Y., DeSmedt, I., Dirksen, R., and Eskes, H. J.: Validation of urban NO2 concentrations and their diurnal and seasonal variations observed from the SCIAMACHY and OMI sensors using in situ surface measurements in Israeli cities, Atmospheric Chemistry and Physics, 9, 3867-3879, 2009.

Browne, E. C., and Cohen, R. C.: Effects of biogenic nitrate chemistry on the NOx lifetime in remote continental regions Atmospheric Chemistry and Physics Discussions, 12, 20673–20716, 2012.

Bucsela, E. J., Celarier, E. A., Wenig, M. O., Gleason, J. F., Veefkind, J. P., Boersma, K. F., and Brinksma, E. J.: Algorithm for NO2 vertical column retrieval from the ozone monitoring instrument, Ieee Transactions on Geoscience and Remote Sensing, 44, 1245-1258, 2006.

Dillon, M. B., Lamanna, M. S., Schade, G. W., Goldstein, A. H., and Cohen, R. C.: Chemical evolution of the Sacramento urban plume: Transport and oxidation, Journal of Geophysical Research-Atmospheres, 107, 15, 2002.

Fishman, J., Bowman, K. W., Burrows, J. P., Richter, A., Chance, K. V., Edwards, D. P., Martin, R. V., Morris, G. A., Pierce, R. B., Ziemke, J. R., Al-Saadi, J. A., Creilson, J. K., Schaack, T. K., and Thompson, A. M.: Remote sensing of tropospheric pollution from space, Bulletin of the American Meteorological Society, 89, 805-821, 2008.

Grell, G. A., Peckham, S. E., Schmitz, R., McKeen, S. A., Frost, G., Skamarock, W. C., and Eder, B.: Fully coupled "online" chemistry within the WRF model, Atmospheric Environment, 39, 6957-6975, 2005.

Harley, R. A., Marr, L. C., Lehner, J. K., and Giddings, S. N.: Changes in motor vehicle emissions on diurnal to decadal time scales and effects on atmospheric composition, Environmental Science & Technology, 39, 5356-5362, 2005.

Hudman, R. C., Russell, A. R., Valin, L. C., and Cohen, R. C.: Interannual variability in soil nitric oxide emissions over the United States as viewed from space, Atmospheric Chemistry and Physics, 10, 9943-9952, 2010.

Jaegle, L., Steinberger, L., Martin, R. V., and Chance, K.: Global partitioning of NOx sources using satellite observations: Relative roles of fossil fuel combustion, biomass burning and soil emissions, Faraday Discussions, 130, 407-423, 2005.

Kaynak, B., Hu, Y., Martin, R. V., Sioris, C. E., and Russell, A. G.: Comparison of weekly cycle of NO2 satellite retrievals and NOx emission inventories for the continental United States, Journal of Geophysical Research-Atmospheres, 114, D05302, 2009.

Kim, S. W., Heckel, A., Frost, G. J., Richter, A., Gleason, J., Burrows, J. P., McKeen, S., Hsie, E. Y., Granier, C., and Trainer, M.: NO2 columns in the western United States observed from space and simulated by a regional chemistry model and their implications for NOx emissions, Journal of Geophysical Research-Atmospheres, 114, 29, D11301, 2009.

Lamsal, L. N., Martin, R. V., Padmanabhan, A., van Donkelaar, A., Zhang, Q., Sioris, C. E., Chance, K., Kurosu, T. P., and Newchurch, M. J.: Application of satellite observations for timely updates to global anthropogenic NOx emission inventories, Geophysical Research Letters, 38, 2011.

Levelt, P. F., Van den Oord, G. H. J., Dobber, M. R., Malkki, A., Visser, H., de Vries, J., Stammes, P., Lundell, J. O. V., and Saari, H.: The Ozone Monitoring Instrument, Ieee Transactions on Geoscience and Remote Sensing, 44, 1093-1101, 2006.

McDonald, B. C., Dallmann, T. R., Martin, E. W., and Harley, R. A.: Long-Term Trends in Nitrogen Oxide Emissions from Motor Vehicles at National, State, and Air Basin Scales, Journal of Geophysical Research-Atmospheres, 117, D00V18, 2012.

Murphy, J. G., Day, D. A., Cleary, P. A., Wooldridge, P. J., Millet, D. B., Goldstein, A. H., and Cohen, R. C.: The weekend effect within and downwind of Sacramento: Part 2. Observational evidence for chemical and dynamical contributions, Atmospheric Chemistry and Physics Discussions, 6, 11971-12019, 2006.

Murphy, J. G., Day, D. A., Cleary, P. A., Wooldridge, P. J., Millet, D. B., Goldstein, A. H., and Cohen, R. C.: The weekend effect within and downwind of Sacramento - Part 1: Observations of ozone, nitrogen oxides, and VOC reactivity, Atmospheric Chemistry and Physics, 7, 5327-5339, 2007.

Pollack, I. B., Ryerson, T. B., Trainer, M., Parrish, D. D., Andrews, A. E., Atlas, E. L., Blake, D. R., Brown, S. S., Commane, R., Daube, B. C., de Gouw, J. A., Dube, W. P., Flynn, J., Frost, G. J., Gilman, J. B., Grossberg, N., Holloway, J. S., Kofler, J., Kort, E. A., Kuster, W. C., Lang, P. M., Lefer, B., Lueb, R. A., Neuman, J. A., Nowak, J. B., Novelli, P. C., Peischl, J., Perring, A. E., Roberts, J. M., Santoni, G., Schwarz, J. P., Spackman, J. R., Wagner, N. L., Warneke, C., Washenfelder, R. A., Wofsy, S. C., and Xiang, B.: Airborne and ground-based observations of a weekend effect in ozone, precursors, and oxidation products in the California South Coast Air Basin, Journal of Geophysical Research-Atmospheres, 117, 14, 2012.

Pusede, S., and Cohen, R.: On the observed response of ozone to NO_x and VOC reactivity reductions in San Joaquin Valley California 1995–present, Atmospheric Chemistry and Physics Discussions, 12, 9771-9811, 2012.

Richter, A., Burrows, J. P., Nuss, H., Granier, C., and Niemeier, U.: Increase in tropospheric nitrogen dioxide over China observed from space, Nature, 437, 129-132, 2005.

Russell, A., Valin, L., and Cohen, R.: Trends in OMI NO_2 observations over the US: effects of emission control technology and the economic recession, Atmospheric Chemistry and Physics Discussions, 12, 15419-15452, 2012.

Russell, A. R., Valin, L. C., Bucsela, E. J., Wenig, M. O., and Cohen, R. C.: Space-based Constraints on Spatial and Temporal Patterns of NOx Emissions in California, 2005-2008, Environmental Science & Technology, 44, 3608-3615, 2010.

Russell, A. R., Perring, A. E., Valin, L. C., Bucsela, E. J., Browne, E. C., Min, K. E., Wooldridge, P. J., and Cohen, R. C.: A high spatial resolution retrieval of NO2 column densities from OMI: method and evaluation, Atmospheric Chemistry and Physics, 11, 8543-8554, 2011.

Ryerson, T. B., Trainer, M., Holloway, J. S., Parrish, D. D., Huey, L. G., Sueper, D. T., Frost, G. J., Donnelly, S. G., Schauffler, S., Atlas, E. L., Kuster, W. C., Goldan, P. D., Hubler, G., Meagher, J. F., and Fehsenfeld, F. C.: Observations of ozone formation in power plant plumes and implications for ozone control strategies, Science, 292, 719-723, 2001.

Schoeberl, M. R., Douglass, A. R., Hilsenrath, E., Bhartia, P. K., Beer, R., Waters, J. W., Gunson, M. R., Froidevaux, L., Gille, J. C., Barnett, J. J., Levelt, P. E., and DeCola, P.: Overview of the EOS Aura Mission, Ieee Transactions on Geoscience and Remote Sensing, 44, 1066-1074, 2006.

Stavrakou, T., Muller, J. F., Boersma, K. F., De Smedt, I., and van der A, R. J.: Assessing the distribution and growth rates of NO(x) emission sources by inverting a 10-year record of NO(2) satellite columns, Geophysical Research Letters, 35, 2008.

Stephens, S., Madronich, S., Wu, F., Olson, J. B., Ramos, R., Retama, A., and Munoz, R.: Weekly patterns of Mexico City's surface concentrations of CO, NOx, PM10 and O-3 during 1986-2007, Atmospheric Chemistry and Physics, 8, 5313-5325, 2008.

Thornton, J. A., Wooldridge, P. J., Cohen, R. C., Martinez, M., Harder, H., Brune, W. H., Williams, E. J., Roberts, J. M., Fehsenfeld, F. C., Hall, S. R., Shetter, R. E., Wert, B. P., and Fried, A.: Ozone production rates as a function of NOx abundances and HOx production rates in the Nashville urban plume, Journal of Geophysical Research-Atmospheres, 107, 4146, 2002.

Valin, L., Russell, A., Bucsela, E., Veefkind, J., and Cohen, R.: Observation of slant column NO2 using the super-zoom mode of AURA-OMI, Atmospheric Measurement Techniques, 4, 1929-1935, 2011a.

Valin, L., Russell, A., Hudman, R., and Cohen, R.: Effects of model resolution on the interpretation of satellite NO2 observations, Atmospheric Chemistry and Physics, 11, 11647-11655, 2011b.

van der A, R. J., Peters, D., Eskes, H., Boersma, K. F., Van Roozendael, M., De Smedt, I., and Kelder, H. M.: Detection of the trend and seasonal variation in tropospheric NO2 over China, Journal of Geophysical Research-Atmospheres, 111, D12317, 2006.

van der A, R. J., Eskes, H. J., Boersma, K. F., van Noije, T. P. C., Van Roozendael, M., De Smedt, I., Peters, D., and Meijer, E. W.: Trends, seasonal variability and dominant NOx source derived from a ten year record of NO2 measured from space, Journal of Geophysical Research-Atmospheres, 113, D043022008.

Table 5.1. Summary of observed and simulated day-of-week patterns of NO_2 column in Los Angeles

		Total NO_2 decrease in Los Angeles[a]	Fraction of Los Angeles Plume[a] where weekend NO_2 decreases		
			> 35%	**> 45%**	**> 55%**
OMI BEHR		**43.0%**	**0.55**	**0.31**	**0.10**
WRF Simulations					
Base	-	**40.4%**	**0.72**	**0.25**	**0.00**
J_{O3}	2×	**43.6%**	**0.55**	**0.36**	**0.12**
	1.5×	42.6%	0.61	0.36	0.04
	1.25×	41.9%	0.66	0.34	0.01
	0.5×	39.2%	0.79	0.09	0.00
E_{VOC}	2×	**42.4%**	**0.66**	**0.36**	**0.03**
	0.5×	39.4%	0.74	0.14	0.00
k_{VOC+OH}	2×	40.9%	0.70	0.28	0.00
	0.5×	40.8%	0.82	0.28	0.00
k_{NO2+OH}	2×	40.6%	0.75	0.27	0.00
	0.5×	40.2%	0.68	0.23	0.00
$E_{weekend}$ **Delay**[b]	2 hr	**44.2%**	**0.74**	**0.43**	**0.01**
	1 hr	42.3%	0.73	0.37	0.00
$E_{weekend}$ **Spatial Dist.**[c]	0.525×	**40.0%**	**0.70**	**0.23**	**0.01**
	0.575×	40.2%	0.71	0.23	0.00

Bold-face entries denote results from simulations shown in Figure 3.

[a] The Los Angeles plume is determined as the region over which the observed weekday NO_2 column exceeds 2.5×10^{15} molecules cm^{-2}.

[b] Both weekend E_{NOx} and E_{VOC} are delayed by 2 hours.

[c] $E_{NOx–S.\ Bernardino}$ is 0.575 ×, 0.525 × $E_{NOx\text{-}NEI2005}$, and $E_{NOx–Los\ Angeles}$ is 0.640 ×, 0.654 × $E_{NOx\text{-}NEI2005}$, respectively, for domain-average weekend emission of 0.625 × $E_{NOx\text{-}NEI2005}$

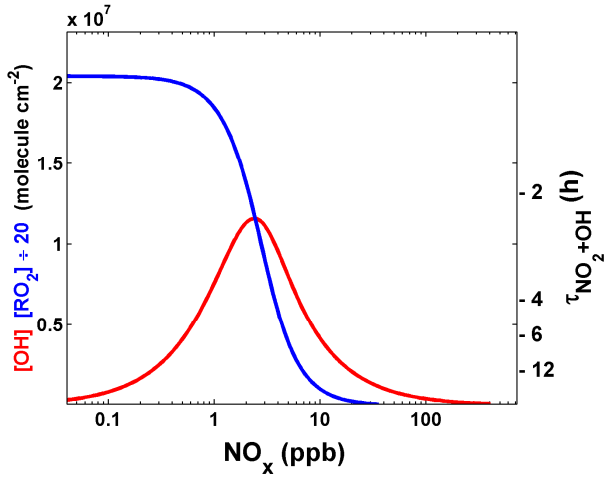

Figure 5.1 The steady-state relationship of OH (red) and RO_2 (÷20; blue) concentrations to the concentration NO_x using the relationship derived in Murphy et al.(Murphy et al., 2006) under conditions typical of a polluted summertime urban environment. The lifetime of NO_x with respect to reaction of NO_2 with OH is indicated on the right axis.

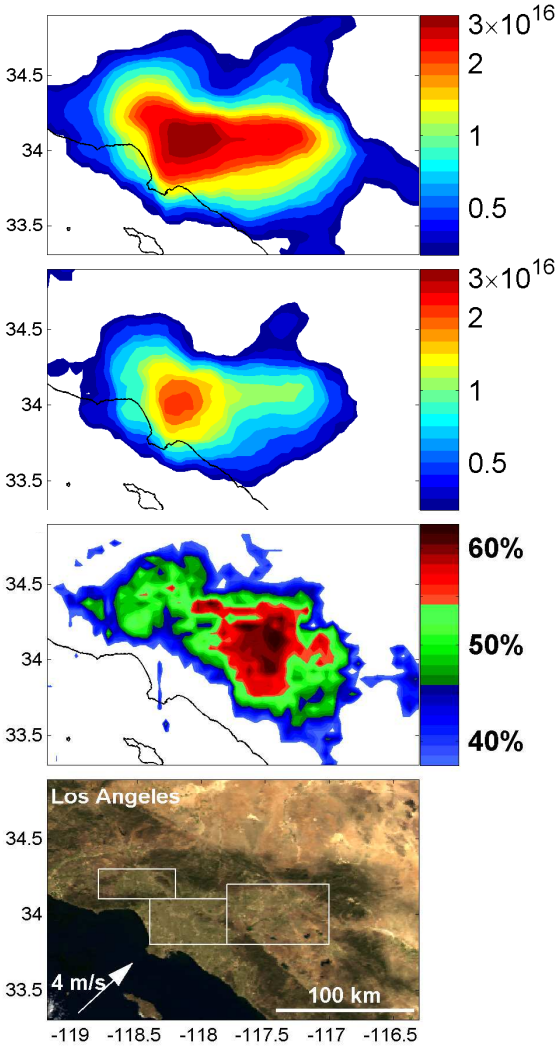

Figure 5.2 May – July, 2005 – 2007 average BEHR NO_2 column for weekdays (top panel) and weekends (second panel), and the percent weekend decrease (third panel). MODIS RGB image of Southern California (fourth panel) with the average North American Regional Reanalysis winds for the region (33.7°–34.0° N; 117.7°–118.4° W) reported in the bottom-left corner, and rectangles marking the San Fernando (NW), Los Angeles (SW) and San Bernardino (E) basins.

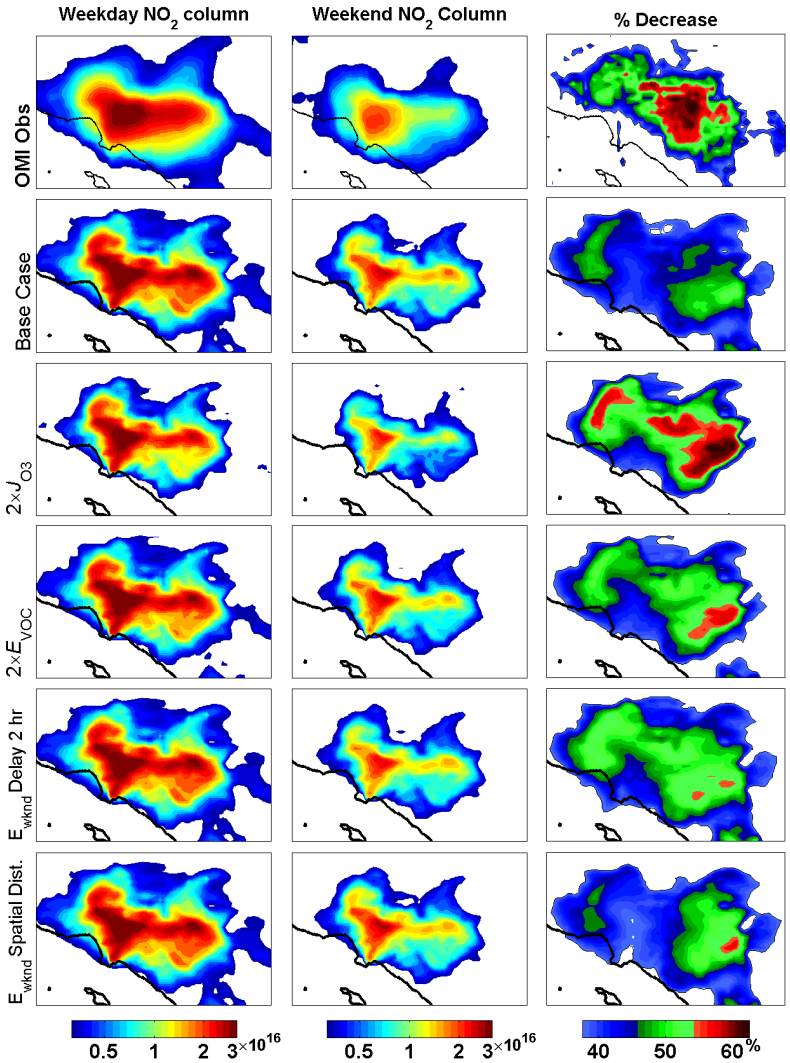

Figure 5.3 Weekday NO_2 column, weekend NO_2 column, and percent change of NO_2 column (top row) observed by OMI for May-August 2005-2008, and simulated with WRF-Chem for 3–14 June 2008 at 1 p.m. LST using a uniform 37.5% reduction in NO_x emissions with standard RADM2 chemistry (second row), a 2× increase of J_{O3} (third row), a 2× increase of anthropogenic E_{VOC} (fourth row), a two-hour delay of anthropogenic weekend E_{NOx} and E_{VOC} relative to weekdays (fifth row), and spatially distinct weekend E_{NOx} reductions (sixth row; Weekend $E_{NOx–San\ Bernardino}$ 0.575×, 0.525× $E_{NOx\text{-}NEI2005}$, and $E_{NOx–Los\ Angeles}$ 0.640×,0.654× $E_{NOx\text{-}NEI2005}$, such that the domain-average weekend E_{NOx} is 0.625× $E_{NOx\text{-}NEI2005}$).

Chapter 6 – Future Directions

In this dissertation, I have explored novel strategies for using satellite-based UV/Vis observations of the NO_2 column measured by OMI with spatial resolution of 13×24 km^2 to enhance our understanding of NO_x sources and the NO_x chemical lifetime.

These analyses are just a beginning. A number of other tests of our understanding should be pursued with these existing measurements. For example, the correlation between water vapor and the NO_2 column that would be expected for situations where OH produced from the reaction of O^1D and H_2O dominates the NO_x sink should be examined. In Figure 6.1, I average the wind-aligned NO_2 column measured by OMI over Riyadh, Saudi Arabia (see Chapter 4 for more details), when surface-level water vapor concentrations are low (< 8 g kg^{-1}), intermediate (8 – 10 g kg^{-1}), and high (> 10 g kg^{-1}). The gradients downwind of Riyadh are much more shallow when the H_2O vapor concentration is low (top panel) than when high (second-panel). Furthermore, there is 35% less NO_2 when H_2O vapor concentrations are high. Both of these observations indicate that the increased H_2O vapor loading decreases the NO_x lifetime.

Other ideas that should be pursued include looking at trends in the NO_x lifetime over the last 7 years, the effects of wind speed in other cities, further examination of weekend effects, and any correlations of the NO_2 column with variations of biogenic VOC emissions, variations of stratospheric ozone that affect O^1D production at the surface, and variations of surface O_3. When performing these analyses, care must be taken to ensure that the independent variable is truly independent. For example, variations of H_2O vapor over Riyadh are independent of wind speed, but springtime variations of stratospheric ozone above the Four Corners power plant are associated with synoptic frontal passages and variations of the surface wind speed.

The other exciting development in the field is the funding of two new high-spatial resolution instruments, the Tropospheric Monitoring Instrument (TROPOMI; launch 2014) and the Tropospheric Emissions: Monitoring of Pollution instrument (TEMPO; launch 2017). TROPOMI is part of a test-phase mission to precede planning for the geosynchronous Sentinel-5 mission over Europe. This precursor mission will operate in a polar-orbit like OMI and will have a 7×7 km^2 footprint at nadir, daily global coverage, and will measure the UV/Visible, near-infrared, and short-wave infrared Earth reflectance, thus providing the means to measure carbon monoxide, CO_2, and methane in addition to what OMI currently measures. TEMPO was awarded funding from NASA's Earth Venture Instrument program in November 2012. It will be hosted on commercial satellite in geosynchronous orbit over North America, 42,000 km above the Earth surface. In geostationary orbit, TEMPO will measure all of North America once each hour with an instrumental footprint of 4.5×2 km^2 (Fig. 6.2), offering unprecedented opportunity to examine patterns of NO_x emissions, chemistry and transport.

These future missions will extend our understanding of the atmospheric chemistry of cities and power plants. Opportunities range from inferring the reaction rate of emitted NO with ozone near a source (5 – 20 km) to forming a better understanding of NO_x chemical processing (i.e., formation of HNO_3, PAN, and $RONO_2$) and the ability to make hourly neighborhood-scale maps of NO_2 concentrations. Perhaps the most exciting outcome of these future measurements will be the capability to distinguish the OH concentration at the plume core, where NO_x concentrations are high from that at the plume edge where NO_x concentrations are lower – a distinction not yet possible even with the best of the current instruments (Fig. 6.3).

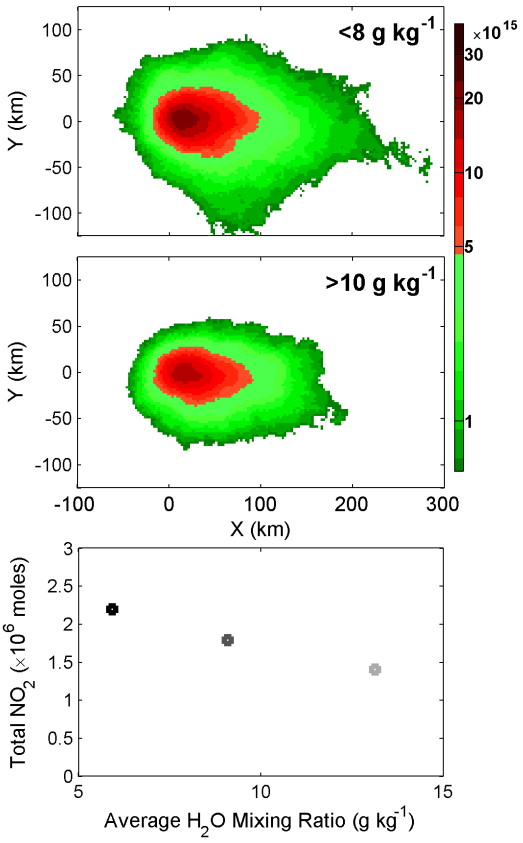

Figure 6.1 The wind-aligned NO_2 column average (see Chapter 4) from October – March, 2005 – 2011 for low (top panel) and high (second panel) surface H_2O vapor loading. (Third panel) The total NO_2 enhancement integrated over Riyadh (x = -100 – 300 km; y = -125 – 125 km) versus average H_2O mixing ratio. H_2O vapor concentrations are from the European Center for Medium Range Weather Forecasting (ECMWF) re-analysis (ERA-Interim) [*Dee et al.*, 2011].

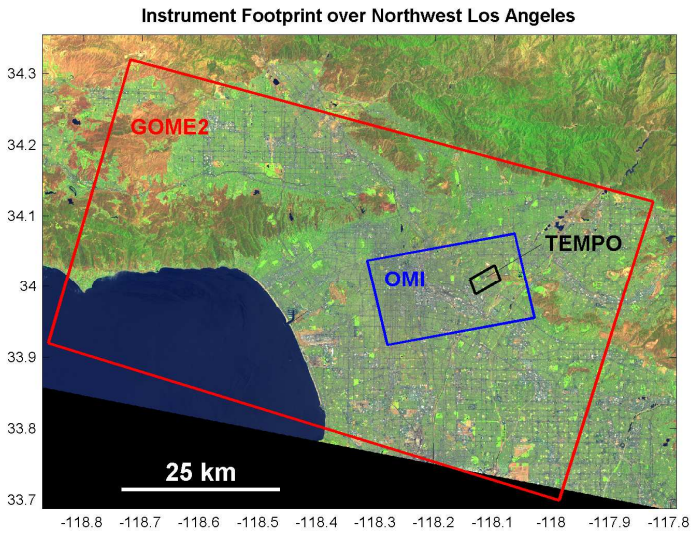

Figure 6.2 The typical nadir instrument footprints of GOME-2 (80 × 40 km^2), OMI (24 × 13 km^2), and TEMPO (2 × 4.5 km^2; launch 2017) on a Landsat false-color image of northwest Los Angeles. GOME-2 and OMI observe each location on the earth at nadir approximately once every other day. TEMPO will observe all of the continental United States and beyond once each hour.

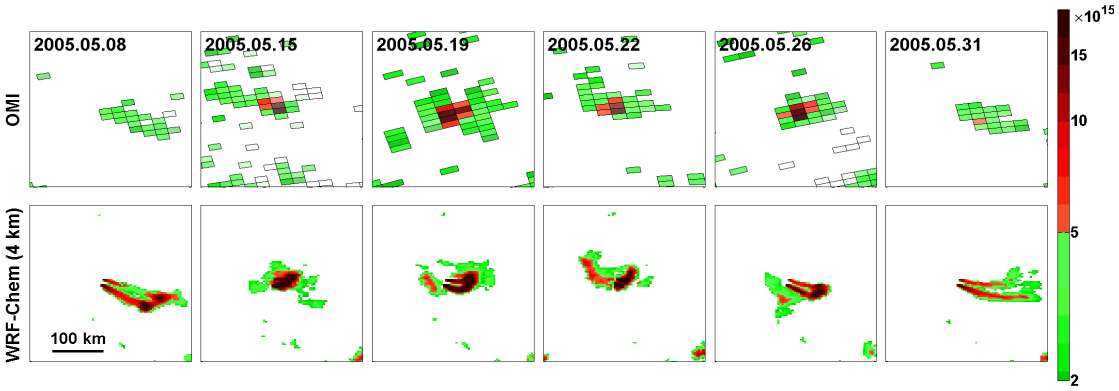

Figure 6.3 (Top 6 panels) NO_2 column for 6 clear-sky near-nadir overpasses of Four Corners, NM, USA (106.5°– 110° W, 35°– 38.5° N) during May 2005 and (bottom 6 panels) the corresponding days 1 PM NO_2 column simulated with WRF-Chem at 4 km horizontal resolution. For the daily measurements, OMI-observed cloud fractions are indicated with transparency: cloud fractions greater than 20% are fully transparent and equal to 0% are fully opaque.